Department of Applied Physics

Fracture propagation and prediction in heterogeneous materials

Juha Koivisto

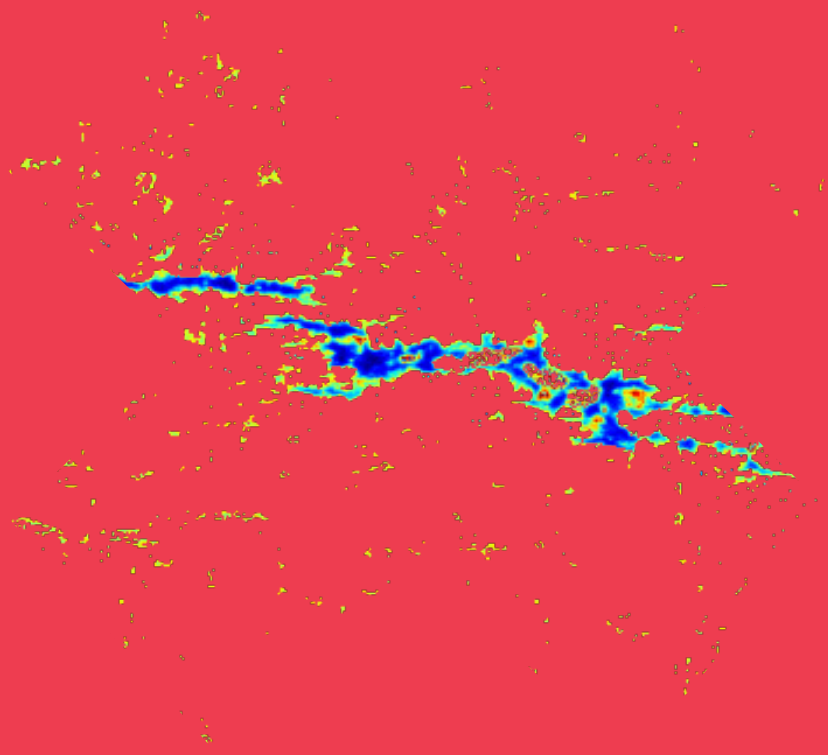

Aalto University

DOCTORAL DISSERTATIONS

Aalto University publication series
DOCTORAL DISSERTATIONS 122/2013

Fracture propagation and prediction in heterogeneous materials

Juha Koivisto

A doctoral dissertation completed for the degree of Doctor of Science (Technology) to be defended, with the permission of the Aalto University School of Science, at a public examination held at the lecture hall E of the school on 4th September 2013 at 12.

Aalto University
School of Science
Department of Applied Physics
Complex Systems and Materials

Supervising professor
Professor Mikko Alava

Thesis advisor
Professor Mikko Alava

Preliminary examiners
Professor Philip Duxbury, Michigan State University, United States
Doctor Juha Merikoski, University of Jyväskylä, Finland

Opponent
Professor Loïc Vanel, Ecole Normale Supérieure de Lyon, France

Aalto University publication series
DOCTORAL DISSERTATIONS 122/2013

ISBN 978-952-60-5275-5 (printed)
ISBN 978-952-60-5276-2 (pdf)
ISSN-L 1799-4934
ISSN 1799-4934 (printed)
ISSN 1799-4942 (pdf)
http://urn.fi/URN:ISBN:978-952-60-5276-2

Unigrafia Oy
Helsinki 2013

Finland

441 697
Printed matter

Aalto University

Abstract

Aalto University, P.O. Box 11000, FI-00076 Aalto www.aalto.fi

Author
Juha Koivisto

Name of the doctoral dissertation
Fracture propagation and prediction in heterogeneous materials

Publisher School of Science

Unit Department of Applied Physics

Series Aalto University publication series DOCTORAL DISSERTATIONS 122/2013

Field of research Engineering Physics

Manuscript submitted 31 May 2013 **Date of the defence** 4 September 2013

Permission to publish granted (date) 19 August 2013 **Language** English

☐ **Monograph** ☒ **Article dissertation (summary + original articles)**

Abstract

The topic of this thesis is fracture and damage. It is discussed with an experimental point of view in multiple geometries.

In Publications I and II a 1D fracture line is driven through elastic medium that is paper. The fracture line propagates with jerky motion producing audible avalanches. These acoustic emission events obey Gutenberg-Richter statistics for energy and Omori law for waiting times.

In Publications III and IV digital image correlation technique is used to measure local strains in paper creep experiments. The significance of local fluctuations increases during the experiment as the fluctuations decay slower than the average strain rate. The global strain rate is found to have a Monkman-Grant relation.

In Publication V the global and local strains are used to predict the failure in the paper fatique experiment. The system is compared to a standard fiberbundle model with viscous components.

Chapter 4 relates to unpublished work of two interacting cracks. Here, it is shown that curved cracks follow the local symmetry path where the shear stress intensity factor $K_{II} = 0$.

Keywords fracture, materials

ISBN (printed) 978-952-60-5275-5 **ISBN (pdf)** 978-952-60-5276-2

ISSN-L 1799-4934 **ISSN (printed)** 1799-4934 **ISSN (pdf)** 1799-4942

Location of publisher Helsinki **Location of printing** Helsinki **Year** 2013

Pages 156 **urn** http://urn.fi/URN:ISBN:978-952-60-5276-2

Aalto-yliopisto

Tiivistelmä

Aalto-yliopisto, PL 11000, 00076 Aalto www.aalto.fi

Tekijä
Juha Koivisto

Väitöskirjan nimi
Murtumisen eteneminen ja ennustaminen kuitumaisten aineiden murtumisessa

Julkaisija Perustieteiden Korkeakoulu

Yksikkö Teknillisen Fysiikan Laitos

Sarja Aalto University publication series DOCTORAL DISSERTATIONS 122/2013

Tutkimusala Teknillinen Fysiikka

Käsikirjoituksen pvm 31.05.2013 **Väitöspäivä** 04.09.2013

Julkaisuluvan myöntämispäivä 19.08.2013 **Kieli** Englanti

☐ **Monografia** ☒ **Yhdistelmäväitöskirja (yhteenveto-osa + erillisartikkelit)**

Tiivistelmä

Väitöskirjan aihe on murtuminen ja vaurio. Tätä käsitellään kokeellisesta näkökulmasta useissa geometrioissa.

Julkaisuissa I ja II yksiulotteinen murtorintama ajetaan läpi elastisen väliaineen, joka on paperi. Murtorintama etenee epätasaisesti tuottaen havaittavaa ääntä. Nämä akustiset tapahtumat noudattavat Gutenberg-Richter statistiikkaa energian suhteen ja Omorin lakia odotusakojen suhteen.

Julkaisuissa III ja IV kuvakorrelaatiotekniikkaa on käytetty paikallisten venymien mittaamiseen paperin virumiskokeessa. Paikallisten venymien merkitys kasvaa kokeen kuluessa, koska venymänopeuden keskihajonta pienenee hitaammin kuin venymänopeuden keskiarvo. Kokonaisvenymänopeudesta löydetään Monkman-Grant suhde.

Julkaisussa V paikallista ja kokonaisvenymää käytetään ennustamaan väsymiskokeen elinaika. Koetta verrataan viskoosiin kuitukimppumalliin.

Kappale 4 liittyy julkaisemattomaan työhön kahden särön vuorovaikutuksesta. Säröt etenevät paikallisen symmetrian osoittamaa polkua. Tällä polulla leikkausvahvistuskerroin on $K_{II} = 0$.

Avainsanat murtuminen, materiaalit

ISBN (painettu) 978-952-60-5275-5 **ISBN (pdf)** 978-952-60-5276-2

ISSN-L 1799-4934 **ISSN (painettu)** 1799-4934 **ISSN (pdf)** 1799-4942

Julkaisupaikka Helsinki **Painopaikka** Helsinki **Vuosi** 2013

Sivumäärä 156 **urn** http://urn.fi/URN:ISBN:978-952-60-5276-2

Preface

First I would like to thank my thesis supervisor Mikko Alava. Thank you for the supervision. I think you have the "try yourself" and "do it like this" in a correct proportion. The goal eventually is to teach me how think on my own and enjoy on the academic freedom on the side.

Science is done as collaboration. This thesis is a good example of that. I would like to thank my co-authors Jari Rosti, Amandine Miksic, Lasse Laurson, Paola Traversa, Xavier Illa, Jean-Robert Grasso, Mikko Alava, Mika Mustalahti and Lauri Salminen. I had also a privilege to work with Stéphane Santucci, Marie-Julie Dalbe and Osvanny Ramos. The pre-examiners Juha Merikoski, Philip Duxbury and the opponent Loïc Vanel deserve thanks for evaluating the thesis.

There exists a number of secondary responsible people that I have had the opportunity to work with. Most of all I would like to thank Jari Rosti for sitting in the same room with me for a number of years and teaching me how not to be a coder, but a programmer. I would like to thank Jari as well as my other room mates Antti Puisto, Lasse Laurson and Amandine Miksic for the physics-and-other-aspects-of-life related discussions that emerged from our room. The other group members namely Matti Peltomäki, Claudio Manzato, Xavier Illa, Wei Chen, Markus Ovaska, Mikael Mohtaschemi, Arttu Lehtinen, Matti Sarjala, Viljo Petäjä, Lei Dong, Hong-Li Zeng, Remi Lemoy, Vesa Väisänen, Roope Kokkoniemi, Marko Korhonen and Shaomeng Qin also reserve a thanks for the same reason.

I was privileged to guide a number of undergraduate students or be otherwise involved through their Bachelor's thesis or similar projects. It was really useful to explain the science behind the projects. The thanks go to Mika Mustalahti, Merli Lahtinen, Niklas Tapola, Julius Vira, Jyri Lehtinen, Simo Seppälä, Emma Mykkänen, Jani Saarenpää, Matleena Myntti, Eetu Pursiainen, Markus Ovaska, Arttu Lehtinen, Ari-Pekka Honkanen, Aleksanteri Mauranen and Tero Mäkinen.

A laboratory needs facilities, for that I would like to thank COMP and its head Risto Nieminen and all the staff, especially Eija Järvinen, Jarkko Salmi and Ivan Degtyarenko for making it possible to work. Also I would like to thank Helena Suvanto and Ville Havu for organising the exams with me. I would also like to acknowledge the financial support from National Graduate School in Materials Physics, Academy of Finland through Centre of Excellence program, VTT and Forest cluster as well as the European Commission NEST Pathfinder program TRIGS under Contract No. NEST-2005-PATH-COM-043386.

For the tertiary people, that are not related to science, I would like to thank my friends Henry Flink, Petri Autioniemi and Mika Joensuu for getting my mind

of things and remembering that there is more to life than distributions. Also for similar reasons I would like to thank Tuomas Koivusalo, Lotta and Paavo Joensuu and Tomi Hietanen.

Finally I would like to thank my mother Helena, father Antti and sister Eija as well as my spouse Anu Vaikinen for moral support.

Contents

List of publications

This Thesis is based on the following original publications, which will be henceforth referred to by the respective Roman numeral.

I Juha Koivisto, Jari Rosti, and Mikko Alava. *Creep of a fracture line in paper peeling*. Physical Review Letters **99**, 145504, 4 pages (2007). DOI: 10.1103/PhysRevLett.99.145504

II Jari Rosti, Juha Koivisto, Paola Traversa, Xavier Illa, Jean-Robert Grasso, and Mikko Alava. *Line creep in paper peeling*. International Journal of Fracture **151**, 281, 17 pages (2008). DOI: 10.1007/s10704-008-9258-7

III Jari Rosti, Juha Koivisto, Lasse Laurson, and Mikko Alava. *Fluctuations and scaling in creep deformation*. Physical Review Letters **105**, 100601, 4 pages (2010). DOI: 10.1103/PhysRevLett.105.100601

IV Lasse Laurson, Jari Rosti, Juha Koivisto, Amandine Miksic, and Mikko Alava. *Spatial fluctuations in transient creep deformation*. Journal of Statistical Mechanics: Theory and Experiment **P07002**, 27 pages (2011). DOI: 10.1088/1742-5468/2011/07/P07002

V Amandine Miksic, Juha Koivisto, and Mikko Alava. *Statistical properties of low cycle fatigue in paper*. Journal of Statistical Mechanics: Theory and Experiment **P05002**, 26 pages (2011). DOI: 10.1088/1742-5468/2011/05/P05002

Author's contribution

The correlation analysis presented in Chapter 2 is unpublished work related to the data in Publication I. Predictability analysis presented in Chapter 3 is unpublished work related to the experiments and simulations shown in Publications III, IV and V. Chapter 4 is based on an unpublished manuscript where the author has done all the analysis and supervised the experiment. The experiments were done by Marie-Julie Dalbe from Université Claude Bernard Lyon 1 and CNRS, Lyon, France. The author is the major developer of the measurement system described in Chapter 5.

Publication I: Creep of a fracture line in paper peeling
Author modified the existing peeling device, performed the experiments and most of the data analysis. Jari Rosti supervised the experimental work and designed the experiment. Mikko Alava wrote most of the paper.

Publication II: Line creep in paper peeling
Author wrote the experiments section of the paper and did the velocity analysis. Xavier Illa made the simulations and wrote the corresponding part of the paper. Paola Traversa and Jean-Robert Grasso wrote the part concerning earthquakes. Jari Rosti combined the different results in the article and performed the correlation data analysis. This publication discusses the topic of Publication I in more detail.

Publication III: Fluctuations and scaling in creep deformation
Author did the small scale experiments, analysis and wrote the corresponding part. Jari Rosti did the large scale analysis and wrote the corresponding part. Lasse Laurson made the simulations and wrote the corresponding part.

Publication IV: Spatial fluctuations in transient creep deformation
Author had an active role in writing the manuscript. This publication discusses the topic of Publication III in more detail.

Publication V: Statistical properties of low cycle fatigue in paper
Author adapted the simulation code and run the simulations and did the related analysis. Author also wrote the simulation part of the paper and supervised the experiments. Amandine Miksic wrote the experimental part of the paper.

Chapter 1

Introduction

The fracture of material is a challenging topic. It has been studied and exploited since the early man starts to use tools (Figure 1.1). But still 2.5 million years later, some fundamental aspects are unclear. In 2010, the standardization agency ASTM withdraw its standard *E338-03 Standard Test Method of Sharp-Notch Tension Testing of High-Strength Sheet Materials* as it contradicted the current understanding of fracture mechanics. The standard described a test method for sharp notch testing and a measure for sharp notch strength. The standard did not provide a method to measure the absolute fracture toughness that is one of the essential properties in crack propagation. This is an example of the constant development and increasing knowledge in this research field.

Figure 1.2 shows a schematic fracture surface in two cases, "real" and simulated. The surfaces and energy landscapes are in most cases self affine, for example fracture surfaces in paper [2]. This means that there are finer and finer details that in many cases cannot be observed during the experiment.

In the case of paper, there exists a flock scale and fiber thickness. The flock scale is the same size as fiber length, $l_f = 1$ mm and the fiber thickness is the order of $l_t = 10$ µm [4]. The point is that there are bonds between clusters and bonds inside the clusters. Usually bonds between clusters are much weaker than between elements. For example in metals fracture tends to propagate along grain boundaries and lattice planes even if the boundaries are not directly orientated along the expected fracture path indicated by global geometry [5]. It is unclear when the propagating fracture surface follows grain boundaries and when it goes through the grains.

In Chapter 2 the fracture geometry is somewhat surprising. A strip of paper is peeled in half along the major plane of the paper sheet. As an example it is possible to peel an A4 sheet to two sheets of A4s. The fracture geometry in this

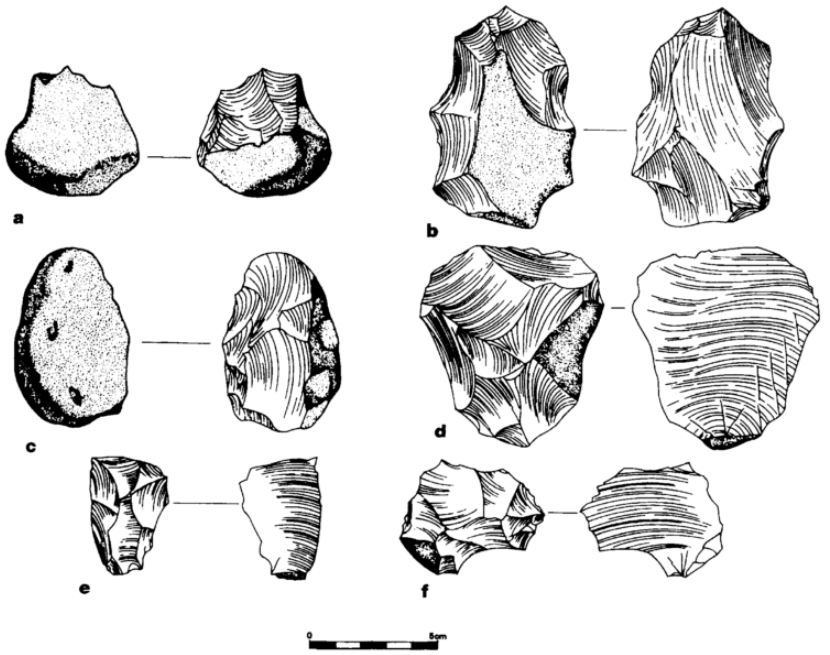

Figure 3 Sketches of a sample of the excavated Gona artefacts. Flaked pieces: **a**, unifacial side chopper, EG12; **b**, discoid, EG10; **c**, unifacial side chopper, EG10. Detached pieces: **d–f**, whole flakes, EG10. Note that the maximum dimension of **d** is as large as some of the flaked pieces.

Fig. 1.1: First known use of fracture properties of materials: stone tools from 2.5 Million years ago. The figure is from Reference [1].

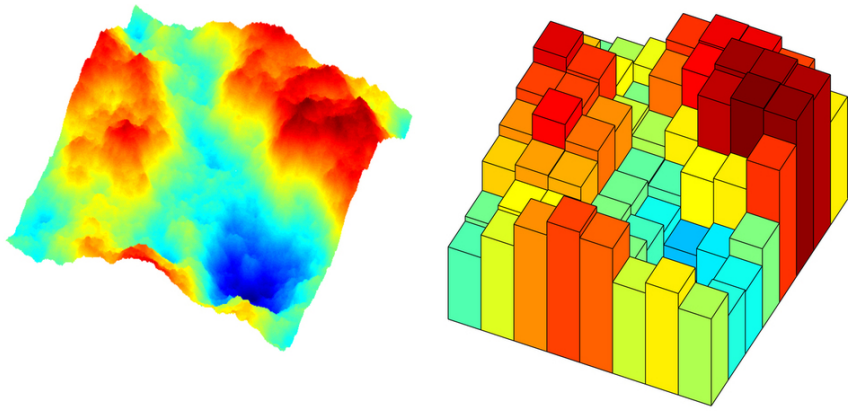

Fig. 1.2: Schematic illustration depicts the difference of real (left) and observed fracture surfaces (right). Direct observation of detailed fractured surfaces is often impossible and averages or indirect observations like acoustic emission have to be used. Surface on the right represents a digitized version (e.g. by digital camera) of the surface on the left. Image is taken from Reference [3].

case is reduced to one dimension. The theoretical point of view is that there is a line interface propagating in an elastic medium. Recent advances in functional renormalization group theory allow the closer examination of this process.

In a different geometry, one can look at the strain concentrations in the surface of a 2D paper sheet. Today, it is possible to analyze local aspects like strains. The fracture problem can be divided into two subcategories: How the fracture initiates and how it propagates. In a given structure, what are the precursors to failures. From the engineering point of view: How long can you use the bridge safely. Prediction of failure is discussed more detail in Chapter 3.

In Chapter 4, fracture propagation is presented with a complex geometry of two interacting cracks. Now the material already has a large enough defect that initiates the crack growth. The question is, where is the crack going to turn, if anywhere. The topic is interesting and challenging at the same time. The fracture mechanics was born at the beginning of the 20th century as Griffith and Irwing studied the growth criteria of elliptic cracks. In linear elastic fracture mechanics, the starting point is the linear elasticity (Hooke's law) and equilibrium equations from continuum mechanics. In the 1950s Williams solved these equations in a plane geometry with a narrow elliptic crack. In his solution the first term is the only non-vanishing one near the crack tip. The prefactor of this

term is called the stress intensity factor K_I in the case of pure tensile loading. The stress intensity factors K_{II} and K_{III} correspond to in-plane and anti-plane shear. These prefactors describe how much less force is needed to break the sample with an existing crack than a sample without the crack.

Since a few years ago the technology has advanced enough for testing these theories. It seems that for simple geometries the theories are correct. It is not so clear in the case of more exotic geometries containing mixed mode loading with tensile and shear stresses. It is experimentally shown in Chapter 4 for the first time that curved cracks propagate along the path where the shear stress intensity factor vanishes. To the authors knowledge there is no previous work where the strain ahead the crack tip has been measured and compared to the crack propagation direction in the case of curved crack paths.

The measurement system developed during this thesis is introduced in Chapter 5. The reason to develop the system was to obtain a way to easily combine many different systems into one. The goal is to synchronize the data and control the devices with ease. Just to mention, adding an existing acoustic emission measurement device to the system took 30 minutes. Creating a control for water heater hardware from scratch was less than a day. During the measurements, the operator can concentrate on the samples and notes. The start and stop are behind one button.

Chapter 2

Peeling

This chapter relates to the papers I *Creep of a fracture line in paper peeling* and II *Line creep in paper peeling*. The author has done the statistical analysis of the experiments with constant load and disorder correlation analysis for both simulations and experiments. Figures from 2.3 to 2.6 and the related text are unpublished work. The goal of this unpublished analysis is to perform a comparison to functional renormalization group (FRG) theory and the renormalized disorder correlator that produces a linear cusp at small correlation lengths. Also, the moments of avalanche size distributions are calculated and compared to ones obtained from FRG theory.

The original experiment set was done with a wide range of weights (driving forces) ranging from 380 g to 533 g. The analysis for the whole experiment set is discussed in References [6] and [7]. The correlation analysis in this chapter concentrates in unpublished results with a subset of experiments that have driving weight around 410 g. The reason for the subset is that with the extreme weights, the events start to appear too sparse or they overlap too much. In both cases the correlation analysis becomes too difficult.

An elastic line pinned in random potential [8] is observed in many physical situations i.e. growth phenomena, domain walls, polymer chains, imbibition or fluid invasion, liquid interface on a solid substrate [9] and fracture fronts. In the last case one can construct a crack that is confined to a plane, for example using an artificial solid-solid interface between two bulks [10]. Or again, one could find a natural crack propagation plane, like in snow avalanches [11] or in ordinary copy paper [7].

More or less in all the fracture cases above the problem reduces to the competition between the disorder and elasticity. In it its simplest form, one has three

forces: i) A random pinning force that tries to keep the system in its local minimum. ii) An elastic restoring force that tries to flatten the surface. iii) A driving force that forces the system to change its state.

In the one dimensional case, the interface is identified as height, h, in a position x. The elastic force generated by the elastic kernel J can be then written as

$$f_{elastic}(x) = \int dx' J(x, x')(h(x) - h(x')), \tag{2.1}$$

The kernel J can be

$$J_{short} = \nabla^2 \delta(x) \tag{2.2}$$

$$J_{long} = \frac{1}{(x - x')^2}, \tag{2.3}$$

where J_{short} corresponds to short range kernel and J_{long} to long range kernel. In Fourier space the former scales as q^2 and the latter as q in a one dimensional case [12]. In the next section experimental realization of the above equations is introduced. Section 2.3 explains the normalization of the data and justifies the comparison between simulations and experiments. The results obtained are compared to theoretical predictions.

2.1 Experiments

The experimental device is introduced in [6, 7]. A 30 mm wide paper sheet is peeled in half along its major plane between two rotating cylinders. This produces roughly a 30 mm wide fracture front which is driven through the sample. The dynamics are intermittent as the driving force is constant.

The average height, $\bar{h}(t)$ and the acoustic emission (AE) is recorded during the experiment. For $\bar{h}$ an Omron laser distance sensor is used. The AE is recorded using standard plate-like piezo sensors and analog preamplification and filtering. The sample rate for both, AE and $\bar{h}$ is 312.5 kHz, but due to noise the data from the distance sensor is averaged over 300 scans, giving it a 1 ms time resolution. The acoustic emission data is processed into t_i, E_i pairs, where a heuristic method is used to identify the event and its energy. The same method is used in References [13, 14, 7, 6]. Figure 2.1 shows an example of the t_i, E_i

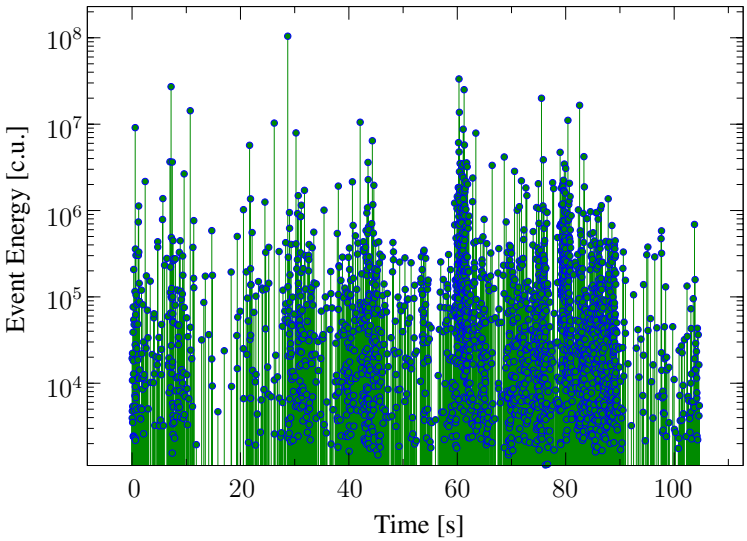

Fig. 2.1: The fracture process creates a set of discrete AE events, an energy time series. Each circle represents an event with energy E_i and time t_i.

timeseries for a single experiment. There is more that ten thousand events per experiment.

A suitable driving mass is around 410 g. For higher masses ($>$ 450 g) the fracture front is constantly advancing (flowing) and for smaller masses ($<$ 400 g) the front is stuck (pinned) for most of the time. Close to the mass 410 g there exists a region where we observe rather symmetric height fluctuations with small enough standard deviation. Fluctuations here mean the difference between the actual front location and the location if the front would advance with a constant speed. In Figure 2.3 the front location is normalized and fluctuations are seen as excursions from the zero level. Let the excursion time be defined as the time it takes the fracture front to pass the expected location of the front (or zero level in Figure 2.3). With small or large driving weights the excursion times become comparable to the experiment duration. This makes the analysis based on autocorrelation difficult as it is expected that the signal is close to zero. The difficulties even with good data can be seen in Figure 2.4 as the disorder correlator ($\sim$ autocorrelation of fracture front height) is oscillating around the

zero level for large values of w.

2.2 Simulations

Experiments are compared to *discrete dynamics* simulations. The simulations are not exactly creep itself but quasi-static. A line segment advances one step, if a random force threshold is exceeded. A more detailed description for the simulations is available in Reference [6]. Technical details can also be found in [15].

Figure 2.2 shows the comparison between event energy distributions for constant force experiments (labeled creep) and simulations. The experiment labeled as "tensile" is a similar experiment but with constant speed [14]. In the tensile experiment the average speed is imposed and the force is measured. Compare this to creep experiment where constant force is applied and speed (location) is measured. The distributions for waiting times $\tau = t_{i+1} - t_i$ and velocity are also similar for all three cases [6].

The event energy distributions shown in figure 2.2 have the form $P(E) \sim E^{\beta}$. The exponent β is found to be $\beta_c = -1.7$ for the creep experiments [7] and $\beta_t = -1.8$ for the tensile experiments [14]. In the simulations the energy exponent is slightly lower $\beta_s = -1.6$. In all cases, the exponents are within the error limits of $\beta = -1.7 \pm 0.1$. The energy exponents are comparable to the burst size exponent found in the similar plexiglass peeling experiment [10].

2.3 Correlation analysis

The goal in this and following sections is to normalize the data in a way that it is possible to compare experiments with different average velocities. The disorder correlator and its third cumulant are calculated in order to compare correlation analysis to measurables obtained from avalanche size distributions. The same measurables can also be calculated from the FRG theory. Similar analysis can also be found in [9], where a silicon or cesium disc is submerged in liquid isobutanol or hydrogen respectively. The substrate-liquid interface forms a contact line that behaves similarly to the fracture front presented here.

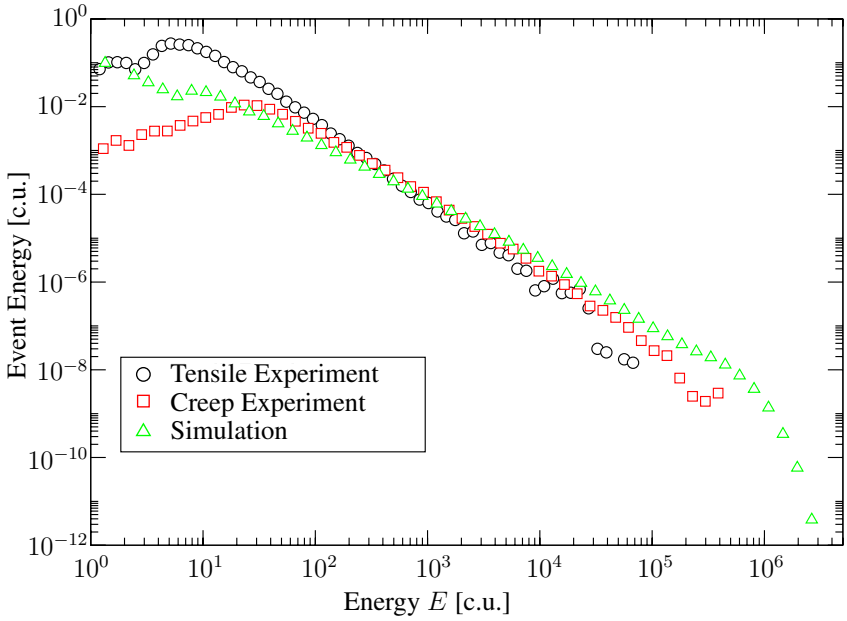

Fig. 2.2: Probability distribution of event energies. The tensile experiment refers to similar experiment but with constant velocity. The figure is reproduced from Figure 6 in Reference [6].

The average interface height, or fracture front location $\bar{h}(t) = \langle h(x,t)\rangle_x$ is a one dimensional time series. Before the heights are compared to other experiments and simulation the height is normalized. First, h', is defined as

$$h'(t) = \bar{h}(t) - v_{ave}t - \langle \bar{h}(t) - v_{ave}t\rangle_t, \tag{2.4}$$

where v_{ave} is the average propagation velocity for each experiment. Second, the time is scaled to distance with average velocity: $w = tv_{ave}$. The outcome is the normalized height, $h_n(w)$, as a function of distance, w with zero mean and trend. Figure 2.3 depicts an example of the normalized height data. A typical experiment is depicted with black. The three simulation cases represent the short, long and periodic-long elastic kernels. In the normalized height, a burst of events is seen as a fast increase in the front height. The event free silent time is seen as the decrease in height.

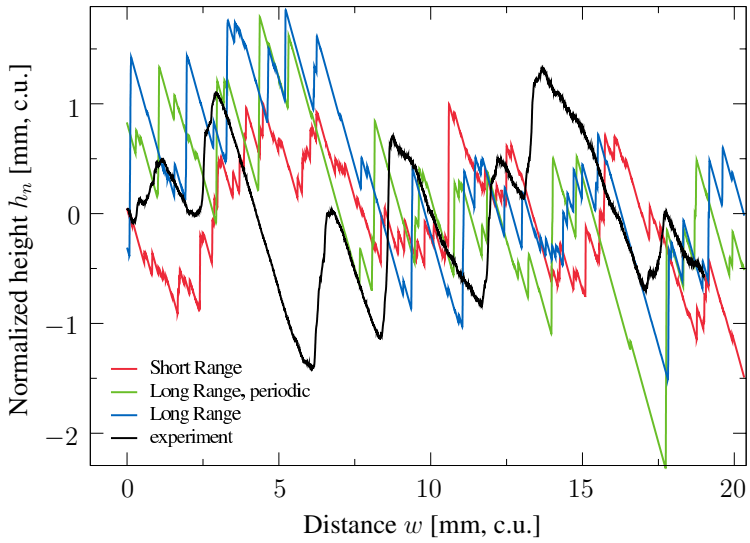

Fig. 2.3: Normalized height, $h_n(w)$ for a single experiment (black) and simulations with short (red), long (green) and periodic-long (blue).

The experimental disorder correlator $\Delta(w)$ for normalized fracture front height is defined as the autocorrelation

$$\Delta(w) = \langle h_n(l) h_n(l+w) \rangle_l. \tag{2.5}$$

The experiments match with a reasonably good accuracy to the simulations. Figure 2.4 depicts the normalized disorder correlator for experiments (solid black line) as well as the simulations (red, green and blue). For experiments the correlation length is about 1 mm. The other experiments labeled cesium and silicon shown in Figure 2.4 are from [9] and scaled to match the experiment (black). All solid lines have a cusp at $w = 0$. The dashed line is the experiment shifted 0.1 mm to the left. This shift illustrates that the slope after the beginning is similar to the simulations, but the beginning is not. The rounding of the cusp at $w = 0$ is most likely due to some correlated phenomena in the measurement device e.g. inertia. Similarly, the negative bump at $w = 2.5$ mm is most likely due to inertia in the device.

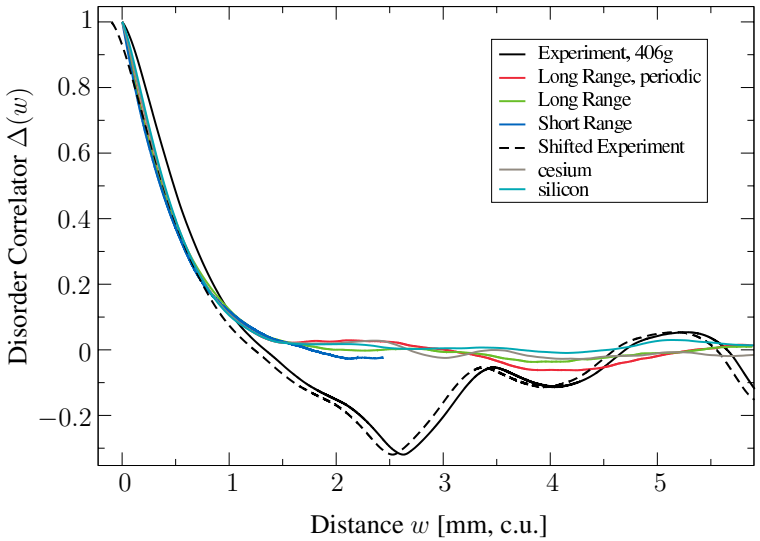

Fig. 2.4: Disorder correlator for simulations and experiments. The peeling experiment is in physical units and others are scaled to match. The data sets labeled cesium and silicon are from [9].

2.4 3rd cumulant

In addition to the disorder correlator Δ it is interesting to examine the third cumulant Q,

$$Q(w) := 1/6 \int_0^w dw' S_3(w') \tag{2.6}$$

$$S_3(w) := \langle (h_n(l) - h_n(l+w))^3 \rangle_l. \tag{2.7}$$

The result is plotted in Figure 2.5. First, the slope, k, obtained from the experiments is close to one half which is in good agreement with theory and simulations. Literature gives values from 0.48 to 0.53 [16, 9]. Second, the short range elastic kernel differs from the long range one. The long range kernel without periodic boundaries matches especially good to cesium experiment.

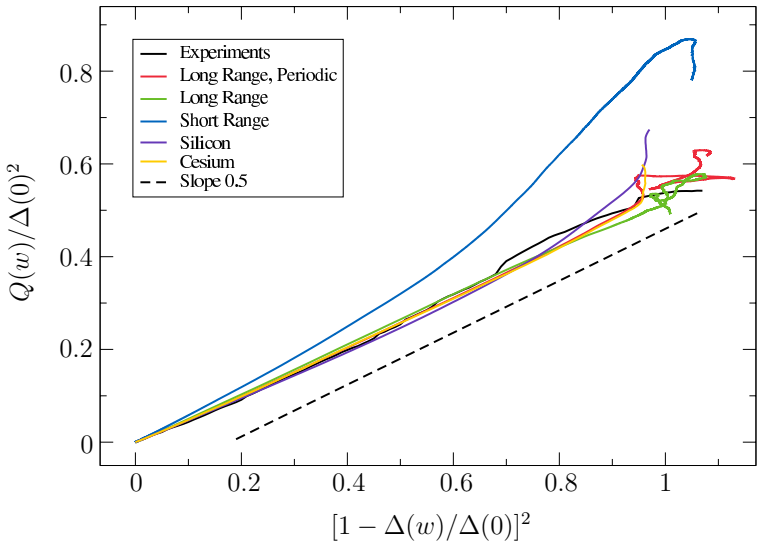

Fig. 2.5: Experiments are compared to simulations using the ratio between first and third cumulants, see Equation (2.6). The simulation with short range kernel differs from all of the others. The experiments labeled cesium and silicon are from [9].

The avalanche size distribution is depicted in Figure 2.6. An avalanche is defined as a group of events between times when front height h_n passes zero level. The avalanche size s is the integral of $h_n(w)$ at the corresponding interval. Figure 2.7 illustrates how the avalanche sizes are calculated.

In Figure 2.6 the distribution is normed such that the integral of first moment equals one and second moment equals two. This gives an alternative way to calculate the slope A in Figure 2.5 [9]. Using

$$A = \langle S^3 \rangle \langle S \rangle / (3 \langle S^2 \rangle^2) \tag{2.8}$$

we get A_{exp} = 0.49, A_{SR} = 0.49, A_{LRl} = 0.51 and A_{LRc} = 0.52. The estimated error for calculation is $\Delta A = 0.05$. Within this accuracy the values agree with

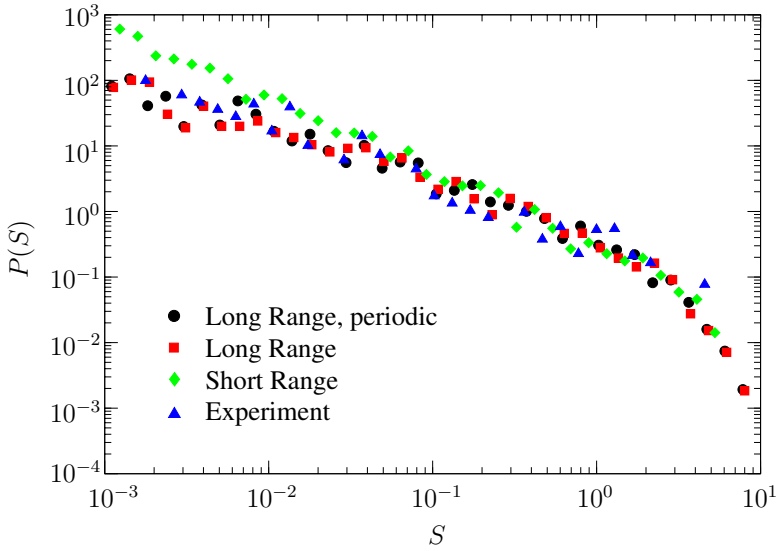

Fig. 2.6: Avalanche size distribution for simulations and experiments. The experiments also better match the long rather than short range kernel, although the difference is not that significant. The figure is courtesy of Xavier Illa.

the slope A in Figure 2.5 except for the short range kernel that has a clearly higher value.

2.5 Discussion

In this chapter it is shown that experimental and numerical realizations of a line interface in random potential have the same characteristics. In publications I and II it is shown that the simulation model has the same energy, waiting time and velocity distributions.

The unpublished material shown here is supporting the observations found in publications I and II. Here, events are observed through the disorder correlator and its cumulants as well as avalanches. The calculated values for A coincide with the literature values that are calculated using FRG theory.

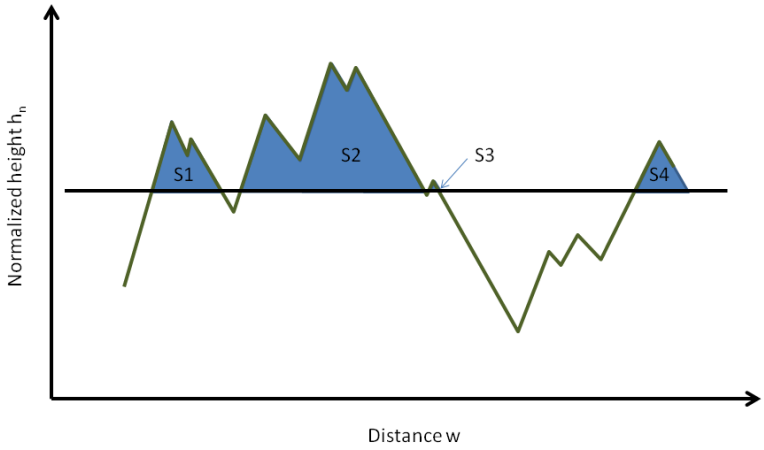

Fig. 2.7: Schematic figure that illustrates how avalanche sizes s_i are calculated. A single avalanche the blue area under the curve with a label e.g. S1. The green line represents the data from experiments or simulations. The black line in the middle is the $h_n = 0$ line.

Chapter 3

Fluctuations and predictability

This Chapter relates to publications III *Fluctuations and scaling in creep deformation*, IV *Spatial fluctuations in transient creep deformation* and V *Statistical properties of low cycle fatigue in paper*. First the localization of damage in paper is introduced and it is used to predict the failure. In the latter part of this chapter, prediction is done using the Monkman-Grant relation [17]. Finally the results are compared to viscoelastic fiber bundle simulations. This Chapter also contains unpublished work that is related to predictability. Figures from 3.5 to 3.10 and the related text have only been presented in conferences. The Monkman-Grant relation in paper creep is introduced in Publication IV.

Time dependent deformation is a difficult topic. The word "creep" itself could also mean Chapter 2 type line propagation in elastic medium as in creep and depinning [8]. However, in this thesis the word "creep" is reserved to the studies of Andrade creep. The name comes from experiment that was done in 1910 by E. Andrade [18]. He took a simple lead wire and loaded it with constant stress. He observed a complex nonlinear response in elongation.

A typical creep experiment can be divided into three parts; primary, secondary and tertiary creep. These regions are identified from their strain rate behavior. In primary creep strain rate behaves as $\dot{\varepsilon} \propto t^{-\theta}$ where $\theta = 2/3$ while here in secondary creep $\theta = 1$. One can also talk about logarithmic secondary creep as strain ε is logarithmic. In the tertiary creep, strain rate increases and sample fails [19].

In paper creep experiments the Andrade exponent of $\theta = 0.7$ and the second Andrade exponent $\theta' = 0.55$ is found [20]. The latter describes the decay of fluctuations, the standard deviation of strain rate. The second Anrade exponent is explained in detail in Publication III. Advances in computer speed and digital imaging have made it possible to obtain the local strains via Digital Image

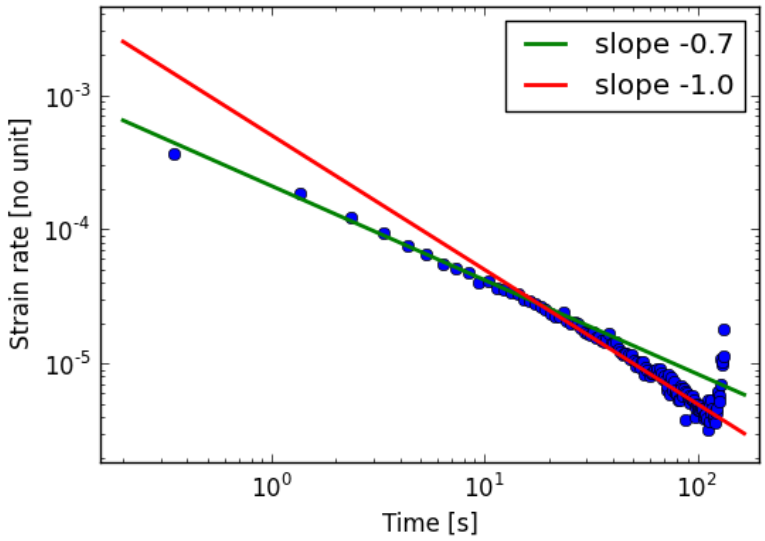

Fig. 3.1: Strain rate of a typical creep experiment (blue dots) illustrates the primary and secondary creep regimes.

Correlation [21]. Figure 3.2 depicts an example of paper sample, where activity sites are visible as high strain regions (red). Similar behavior is found in crystal plasticity underlying the Andrade creep with a jamming or yielding transition [22, 23].

3.1 Localization

In Publication V, the fluctuations are studied not only at the beginning, but throughout the experiment. In this case, the loading protocol is cyclic fatigue with considerably long loading and relaxation times. The number of cycles are measured in tens unlike in more common fatigue testing with thousands or more.

During the experiment the strain concentrates to a few (hot) spots. One of these spots develops into a microcrack that eventually breaks the sample. Despite all the attempts, there seems to be no clear indication during primary creep, which of the spots will develop into a microcrack. Figure 3.3 depicts the primary strain rate ε_{yy} just before failure. The sample fails at the point where strain rate is

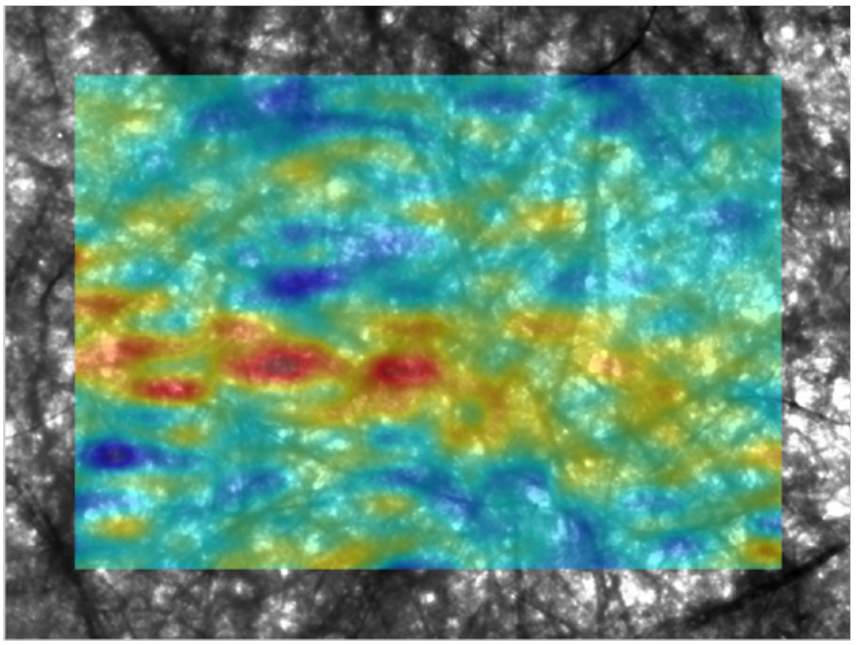

Fig. 3.2: Large magnification of a paper sample with strain as contour plot overlay. The sample has been loaded for 100 seconds. Figure width is roughly 10 mm.

highest (red) in both cases. The increase in fluctuations, strain rate and acoustic emission event rate are tightly connected, but how they are connected is unclear.

3.2 Predictability from the primary creep

In a brittle fracture process the sample-to-sample variation comes from the variation of modulus of elasticity and the tensile strength. These properties are often uncorrelated within the same material. The tensile strength is determined by the development of the critical crack [25] that cannot be predicted [26, 27]. On the other hand, there exists some empirical laws suggesting that the lifetime is in some sense predictable.

In this section it is hypothesized that the areas of high strain are due to existing weak spots, areas of low elastic modulus, low fracture toughness or similar

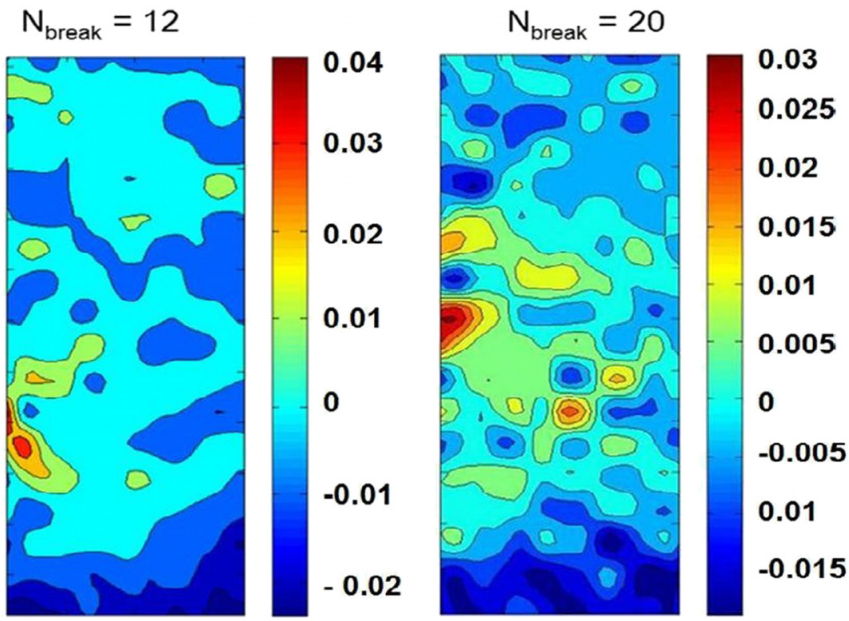

Fig. 3.3: Strain rate ε_{yy} is shown as contour plot just before failure in cyclic creep experiments. N_{break} is the sample lifetime in cycles. Figure is Figure 15 in Reference [24].

material property. These weak areas set the state of the sample at the beginning of the experiment by breaking and determine the behavior of the rest of the experiment. The sample can be thought to have brittle elements that break at the beginning of the experiment creating strain and stress concentrations or even microcracks. These strain concentrations can be measured and make it possible to predict what happens next to the sample.

In this thesis predictability means the ability to predict what is the lifetime of the sample. The goal is to predict this at the earliest possible time. In previous sections, Andrade creep was found to have some general features. These features can be used to estimate the lifetime of the sample. The samples related to this section are standard 80 g/m^2 copy paper sheets with dimensions of 100 x 50 mm. The load is usually constant 75 N applied within 5 seconds.

Lifetime is predictable from the beginning of the experiment. The primary to secondary creep transition versus time is shown in Figure 3.1. The figure shows a typical strain rate as a function of time with blue dots. The two lines indicate

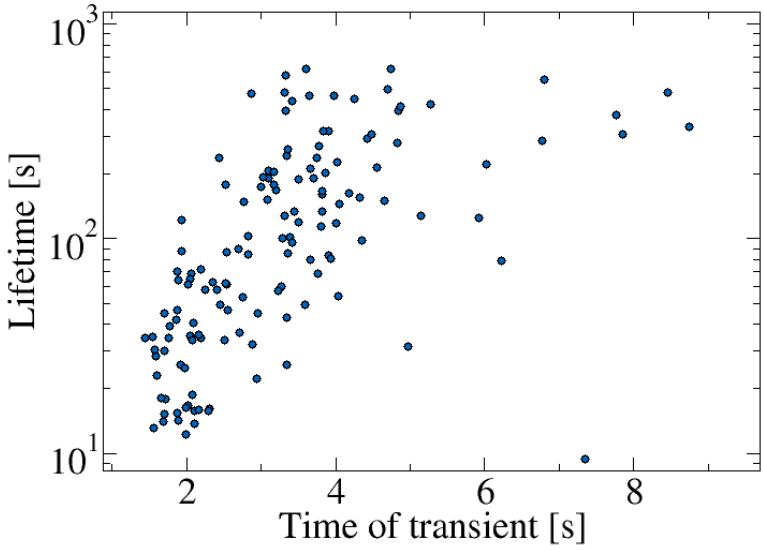

Fig. 3.4: The transition from primary to secondary creep region correlates with lifetime. See Figure 3.1 for illustration of the transition.

the slopes that are expected for primary and secondary creep.

The time of transition t_{trans} from primary creep to secondary creep can be defined in many ways. Here, the strain rate vs time data is fitted with theoretical Andrade creep $\dot{\varepsilon}_{fit} = at^{-2/3}$. The values of t start from the beginning of the experiment and end with t_{trans}. The transition time t_{trans} is the largest time for one which the error between the fit and data is less than 10 %. In other words, increase the fit region until the error is larger than 10 %. This method is comparable to the usual methods how the yield point is calculated from stress-strain data. However, the existing correlation is not strong.

The method explained above uses information only from the beginning of the experiment and can predict the order of magnitude for the sample lifetime. Figure 3.4 shows that after ten seconds all the lifetimes can be estimated. For example, if the transient time t_{trans} is less than 2 seconds, the experiment will last tens of seconds. If the transient is larger than 4 seconds, the experiment will last hundreds of seconds.

Fluctuations, defined as standard deviation of strain rate, also correlate with lifetime. Figure 3.5 shows the ratio of standard deviation per strain rate versus lifetime. Here, the ratio is calculated at a fixed time of t_r = 128 s from the beginning. The result leads to rather expected conclusion. If the standard deviation of strain rate is large, the sample has a small lifetime. This means that there exists either one or more areas with high strain rate. It is reasonable to assume that the area of high strain rate leads to microcracking and failure of the sample.

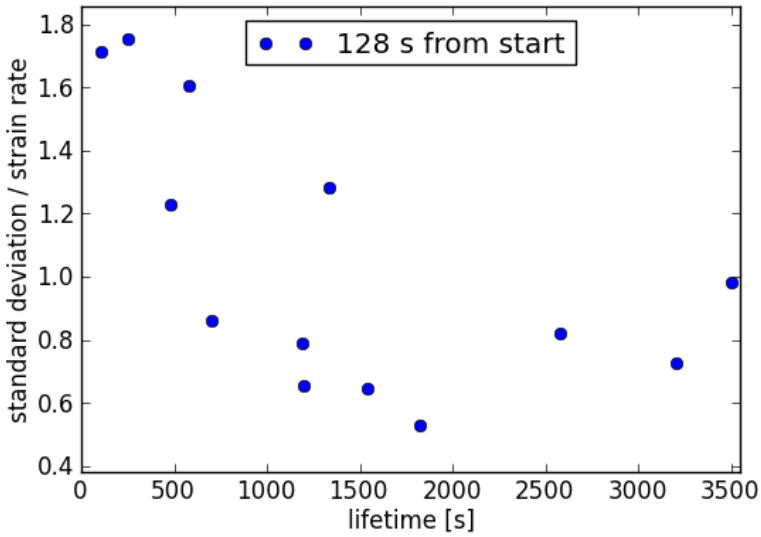

Fig. 3.5: Fluctuations at the beginning correlate with lifetime

3.3 Monkman-Grant relation

Creep fracture often includes both phenomena: strain hardening and softening. In constant loading, the strain rate first decreases (hardening) after which the strain rate increases. This produces a minimum strain rate.

The Monkman-Grant (MG) relation is an empirical result between minimum strain rate and lifetime in a creep experiment. It was discovered by Monkman and Grant in the 1950s when studying the creep of metal alloys [17]. Nowadays MG relation is a standard concept tool when studying metal alloys under

constant loading. The original relation states that ratio between minimum strain rate $\dot{\varepsilon}_{min}$ and lifetime t_c to a power γ is a constant,

$$\dot{\varepsilon}_{min} = C t_c^{-\gamma}. \tag{3.1}$$

Figure 3.6 depicts the original MG relation with the value of $\gamma = 1.2$ for paper experiments.

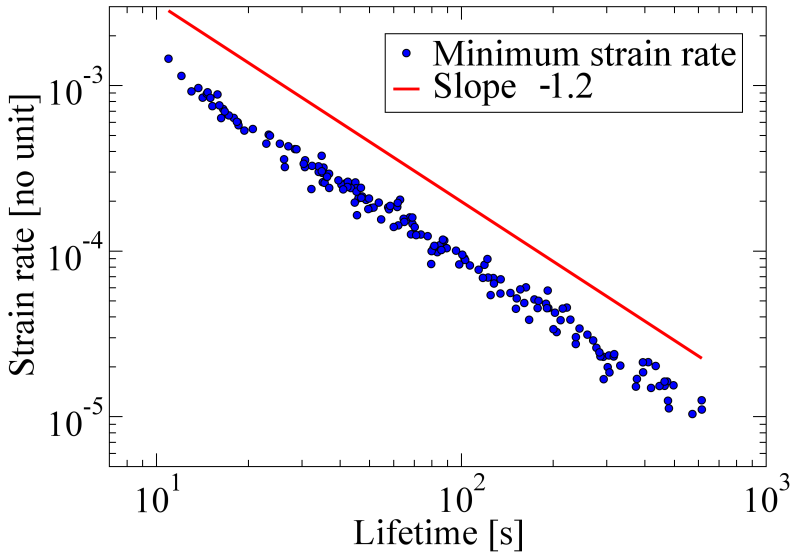

Fig. 3.6: Monkman-Grant relation applies for a wide range of experiments. Each dot is an individual experiment.

In engineering literature the above equation is usually given in the form

$$t_c \dot{\varepsilon}_{min}^m = C'. \tag{3.2}$$

The exponent γ is usually close to one, for metals it is found to be $\gamma = 1.05 \ldots 1.25$ ($m = 1/\gamma = 0.8 \ldots 0.95$). The value of C' for metals is typically $C' = 3 \ldots 20$ [17].

There exists also a modified Monkman-Grant relation:

$$\frac{t_c \dot{\varepsilon}_{min}^n}{\varepsilon_c} = C'', \tag{3.3}$$

where ε_c is the strain at failure and n is close to unity. More recently [28], a relation between time of minimum strain rate t_m and lifetime has been used as

$$t_m = C' t_c^{\beta}. \tag{3.4}$$

β is typically above one giving slightly convex i.e. slope increases with lifetime t_c.

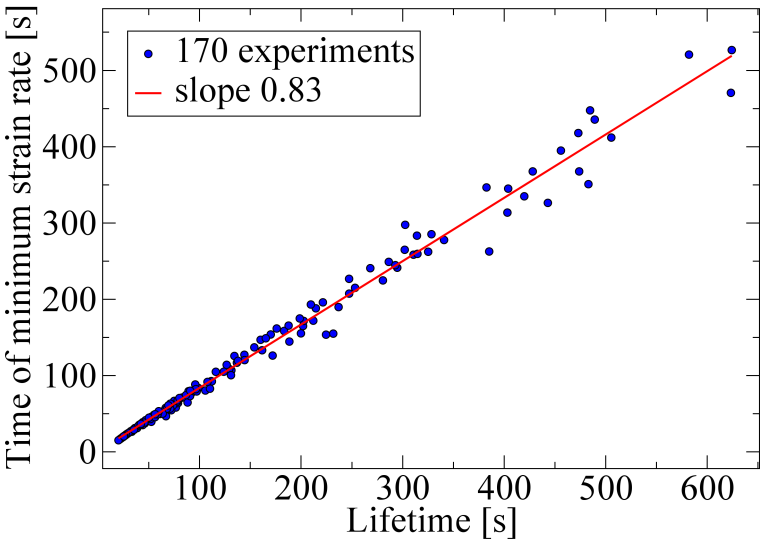

Fig. 3.7: A modified Monkman-Grant relation gives the value of 0.83 for the ratio of t_m/t_c. The dataset is the same as in Figure 3.6.

In Figure 3.7, Monkman-Grant relation is presented as fraction of lifetime: Time of minimum strain rate t_m versus lifetime t_c. This yields the relation

$$t_m = 0.83\ t_c. \tag{3.5}$$

Notice that for small lifetimes t_c there is slightly convex behavior that can be interpreted as $\beta > 1$ c.f. equations (3.4) and (3.5) with Figure 3.8. However, the 5 second loading ramp is a large portion of the small lifetimes. Adding a part of loading time to the lifetime removes the upward curvature and lets to set $\beta = 1$.

Changing the loading protocol has no effect on the Monkman-Grant relation. Figure 3.8 depicts the Monkman-Grant relation for creep with preloading as well as different loads. Preloading before fatigue testing can even reduce the amount of damage accumulated during the actual experiment if the preload is close to ultimate tensile strength [29].

The lack of sensivity to both relaxation and load indicates that the memory effect is very small. In other words, there are either completely irrecoverable changes in material, or very slow delayed elastic recovery (large viscosity in relaxation).

3.4 Discussion and models

In this section the creep behavior of paper is explained by constructing a model that tries to capture the essential features of the experiment. The model does not need to be that difficult. In its simplest form only two processes can be assumed. A stable process with decreasing strain rate combined with unstable process with accelerating strain rate produces qualitatively the same behavior [30] what is seen is a standard creep curve in Figure 3.1.

The following model explains the MG ratio and localization of strain observed in the experiments. Acoustic emission at the end indicates that the accelerating process is brittle failure [24]. Brittle failure can be explained by standard fiber bundle model, most recently used in [31]. In a simplest fiber bundle model, perfectly brittle elements (spring) in parallel are under increasing load. Fibers break if they are elongated beyond their breaking threshold, ε_t. The load is shared equally with unbroken elements, i.e. global load sharing [32]. The above models brittle solids. One can capture ductile behavior by extending a simple fiberbundle model with time dependent behavior. Adding a dashpot allows the modeling of constant loading [33]. Even further, adding spatial structure makes it possible to model local strains.

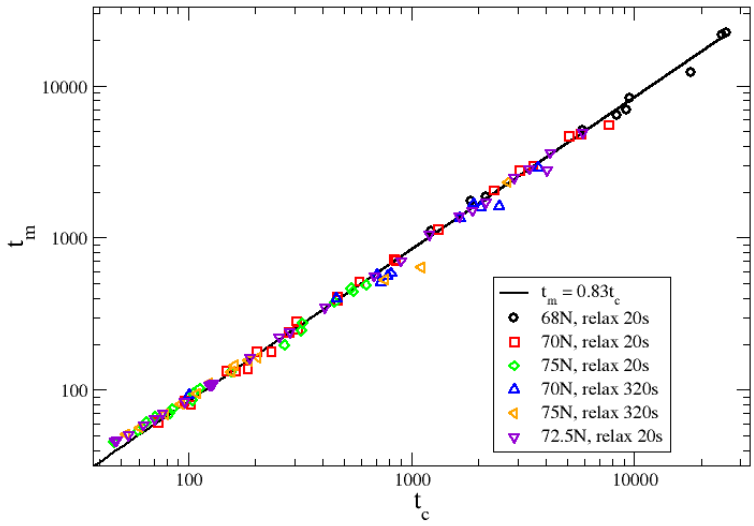

Fig. 3.8: A Monkman-Grant relation does not change if there is a preloading with a relaxation period. In the experiments, there is a 20 second loading period followed by 20 (or 320) second relaxation period with no loading before the creep experiment. This seems to have no significant effect on the Monkman-Grant relation. The figure is courtesy of Markus Ovaska.

Figure 3.9 shows the Monkman-Grant ratio of single viscoelastic fiberbundle similar to experiments, Figure 3.7. The Monkman-Grant ratios are close to one half and don't depend much on which kind of distribution for failure thresholds are used. With the standard fiberbundle model the MG ratio is $r_{MG} = 0.5$ [31]. To get closer to experimental value of $r_{MG} = 0.83$ the model is changed to have multiple independent fiberbundles in series. As the number of bundles in series N increases the MG ratio changes from 0.5 towards 1. Figure 3.10 depicts the Monkman-Grant ratio for different number of fiber bundles in series. The MG ratio of $r_{MG} = 0.83$ corresponding to experiments is obtained with $N = 20$ bundles. In the experiments, the typical microstructure scale, "the flock size" is the order of 1 to 2 mm. In a 100 mm long sample there exists tens of individual fracture initiation sites, not hundreds nor one.

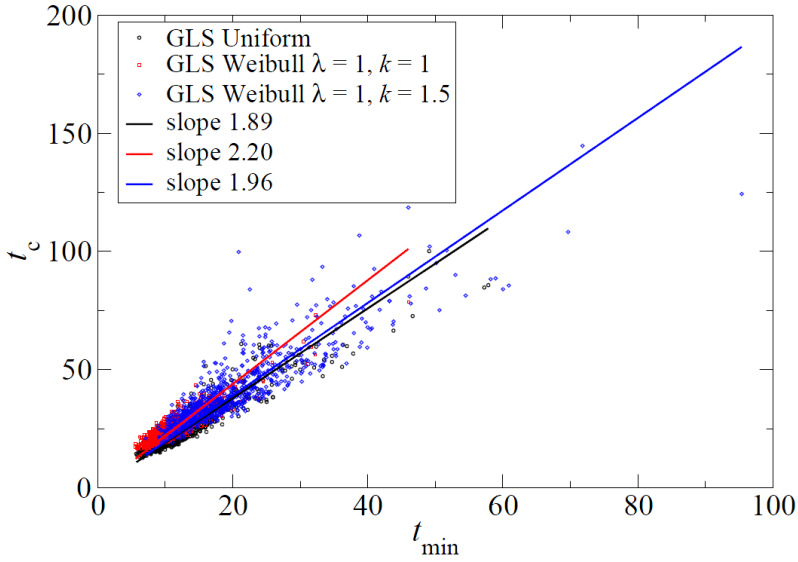

Fig. 3.9: The Monkman-Grant ratio is depicted for three different breaking threshold distributions with global load sharing (GLS). In all cases the MG ratio is close to $t_m/t_c = 0.5$. The figure is courtesy of Lasse Laurson.

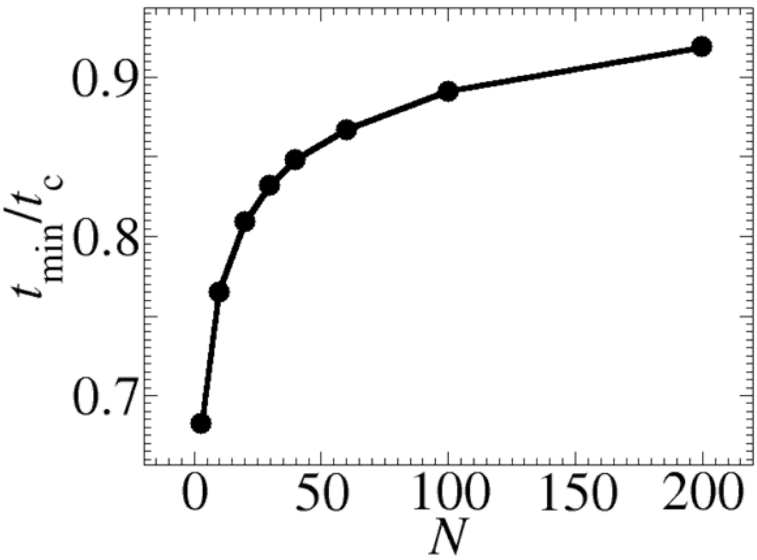

Fig. 3.10: Evolution of Monkman-Grant relation as a function of the number of fiberbundles in series N. The figure is courtesy of Lasse Laurson.

Chapter 4

Fracture from cracks

This chapter overviews an unpublished manuscript about crack propagation. The main geometry is a double notched sample seen in Figure 4.1, where cracks propagate towards each other slightly off axis. The geometry allows the inspection of local symmetry arguments in mixed mode loading. The goal is to show that the shear stress intensity factor, K_{II} vanishes along the crack trajectory. This approximation is valid for small deviations from straight path [34]. The two crack geometry forces large deviations and finally in some point the local symmetry approximation fails. At least, when the samples go out of plane and start to buckle. Also, the two crack case is a dynamical process where the interacting cracks form a sort of feedback loop that determines the crack path.

Recent advances in photoelasticity allow the examination of stress fields [35]. From this study, an experimental verification between K_{II} and crack direction is obtained. However, the interpretation of photoelastic results is still difficult. The approach used here is based on strains obtained from digital image correlation, but the idea is the same: At any given time, what is the crack propagation path and how far is it valid?

There has been a few papers, where the validity of linear elastic fracture mechanics (LEFM) and local symmetry arguments is questioned [5, 36]. On the other hand, in some other papers the theory works perfectly [37, 38]. The catch is that standard LEFM fails and higher order terms are needed.

In mixed mode loading the crack path becomes curved. There is a somewhat famous experiment by Nooru-Mohammed [39] showing curved trajectories. The path of the trajectories are aposteriori simulated [37, 40] using finite elements. However, the strains during the crack propagation are not recorded, only the final crack path. In this chapter, the goal is to create a curved crack path by two

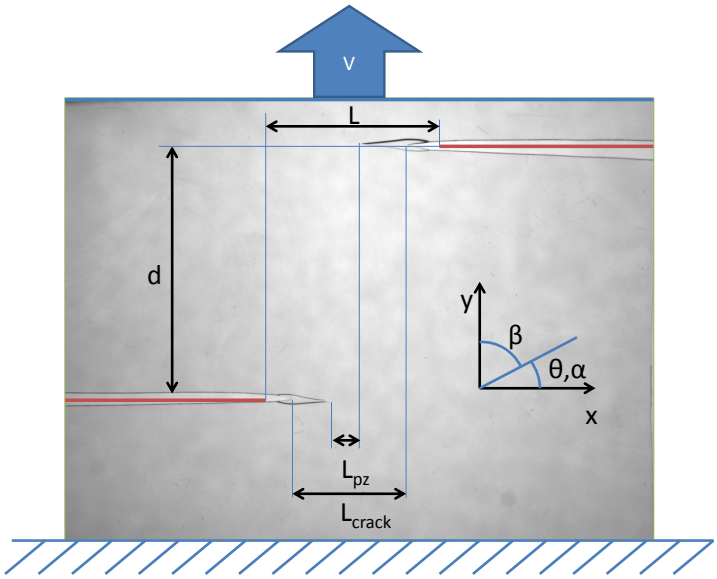

Fig. 4.1: Schematic illustration shows the sample geometry. Initial notches are depicted with red and their initial distances are labeled as L for horizontal and d for vertical. The horizontal distances between cracks and plastic zones are noted with symbols L_{crack} and L_{pz} respectively. The tension is applied with a constant velocity of $v = 0.02$ mm/s. β is the angle between the applied tension and initial notches. α is the complement of β. θ refers to the angle of the propagating plastic zone respect to horizontal axis.

interacting cracks and compare the experimental strains to static finite element simulations as well as elasticity theories.

4.1 Material and methods

The experiments are done with polycarbonate sheets. Polycarbonate as a test material is easy to use. It has a convenient property of a clearly visible yield zone or fracture process zone (FPZ) [41]. Outside this zone material can be approximated as purely elastic with good accuracy.

The dimensions of the sheet are w x h x t = 100 x 120 x 0.1 mm. A snapshot of a typical experiment is depicted in Figure 4.1. The plastic zones have grown and are interacting with each other. In this case $d = 40$ and $L = 20$ mm. The sample is notched from two sides symmetrically with two tunable parameters: horizontal L and vertical d notch distances illustrated in Figure 4.1. The vertical distance is fixed to $d = 40$ mm and the horizontal distance is varied $L = 10, 20, 40, 60, 80$ mm. The transparent sample is painted with inert water-based paint. This is to help the digital image correlation algorithm. The images are recorded by a standard digital grayscale camera Dalsa HM1024.

The sample is attached to a standard tensile testing machine, Instron Electropuls 1000. The orientation of the sample is such that the primary stress and strain are perpendicular to the notches depicted in Figure 4.1. The effective testing area is 100 x 100 mm due to 10 mm material reserved for clamping. The testing machine imposes a constant displacement speed of $v = 0.02$ mm/s to the upper crosshead. The machine stores the force-displacement data with a frequency of $f = 500$ Hz.

The analysis of the experimental data relies on two methods. First, the plastic zone tip location is obtained via conventional edge detection. Second, the displacement field is obtained using digital image correlation algorithm. The algorithm is explained in detail in [21] and is used also in [20].

The polar displacements u_r, u_θ are calculated by projecting the Cartesian displacements to a polar base. The tangential (hoop) strain $\varepsilon_{\theta\theta}$ is a numerical derivative of tangential displacement u_θ respect to θ. Cartesian displacements are obtained from the above mentioned digital image correlation algorithm.

Here, the strain components are measured in a time window of Δt = 2 s. The word strain is used instead of strain rate because the strain near the crack tip during the 2 seconds contains most of the strain that the material is going to experience.

4.2 Local symmetry theory

There exists multiple ways to determine the crack growth direction [42]. A comparison between crack propagation criteria is given for example in Reference [43], where four methods are considered: i) maximum tangential stress, ii) maximum tangential strain (MTSN), iii) maximum tangential principle stress and iv) strain energy density criterion. The derivation of the methods and the initial assumptions are different but the results are the same when the cracks are

propagating in the same direction as the initial crack ($\beta = \theta = 90\,\mathrm{deg}$ in Figure 4.1).

From the theoretical data of [43] one can conclude that when an angle of a crack β is more than 75 degrees (or $\alpha \leq 15\,\mathrm{deg}$), all methods give the same result for crack propagation angle within 2 degrees. That is, all methods give same results if the propagation direction is close to horizontal in a geometry described in Figure 4.1. Also, Cottrell and Rice [34] conclude in their paper that maximum tangential stress (or similar) criteria essentially mean that the stress intensity factor K_{II} vanishes at the propagation direction. This is called the local symmetry argument. Note that the local symmetry argument holds again for small angles $\alpha < 15\,\mathrm{deg}$.

Here, the hypothesis is that given a random initial crack geometry (or a heterogeneous material) the crack propagation direction obeys the local symmetry argument. As the stress of a homogeneous material is difficult to measure, an approximation is made that the maximum tangential strain criterion estimates the same propagation angle as the maximum tangential stress.

In the case of simple two crack geometries, the K_{II} component can be calculated analytically. Usually, the value is calculated as if the crack would propagate horizontally, like in Figure 4.2. It is found that K_{II} is positive when the ratio d/L is small and negative when d/L is large [45, 44]. In other words, the shear component causes first repulsion and then attraction as the crack propagates. An interesting notion is that $K_{II} = 0$ in two cases. Either both cracks lie exactly on the same (horizontal) propagation axis or when the ratio horizontal/vertical crack separation has the value $d/L \approx 2$.

The above has two implications, head-to-head geometry is unstable and cracks seem to avoid each other [46]. In the interval $d/L \in]0, 2.0]$ there exists a repulsive region which turns to attractive region above $d/L = 2.0$. In the experiments (e.g. Figure 4.4). We see the same behavior. As d per L ratio decreases below 2, the repulsion turns to attraction.

Figure 4.3 depicts the vertical strain rate ε_{yy} for repulsive geometry (left), turning point (middle) and an attractive geometry (right). Figure 4.3 is just for schematic purposes, underlining the connection between local symmetry, repulsion/attraction and mode II stress intensity factor K_{II}. In the repulsive geometry (left) the ratio is $d/L = 1$ and the K_{II} gets positive values indicating repulsion. The black line represents the symmetry axis of the yy-strain ε_{yy}. In the middle figure the ratio is $d/L = 2$ and the symmetry axis is horizontal. In this case the value of $K_{II} = 0$ and the crack is propagating horizontally. In the figure on the right the ratio is $d/L = 5$ and the two cracks are attracting each other. In this case the black symmetry line points downwards and the K_{II} is negative.

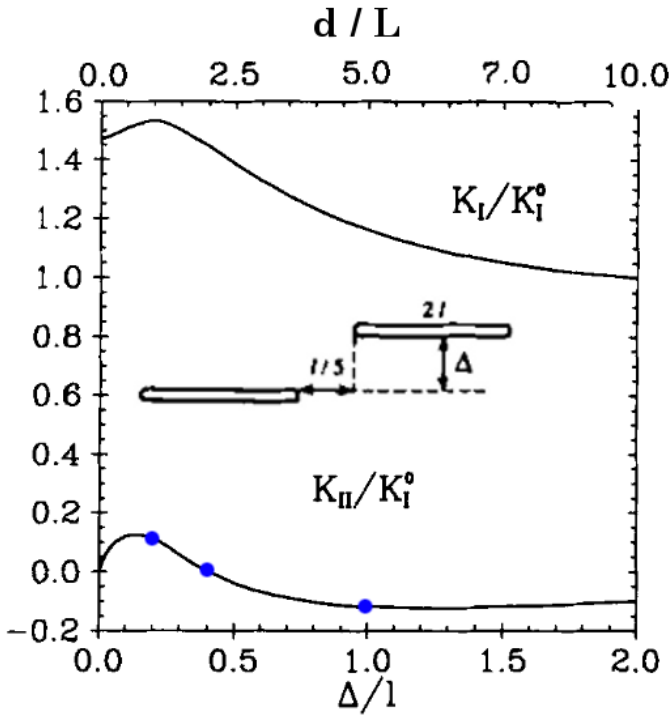

Fig. 4.2: Analytical calculations indicate that when the ratio d/L is small, cracks repel each other. The figure is reproduced from Reference [44].

Experimentally, observing repulsion and attraction is seen in some material but not others. Fender et al. [47] report that interaction starts just after the cracks pass each other ($L_{crack} = 0$ in Figure 4.1) indicating that K_{II} is always positive, in other words there is no repulsion, just attraction. They also report an universal shape for the crack paths in the attractive region for a wide range of materials consisting metals, plastics and gels.

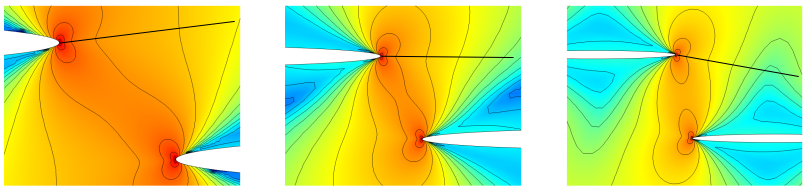

Fig. 4.3: ε_{yy} is shown as contour plot for the geometry described in Figure 4.1. The data is obtained from finite element simulation of a thin polycarbonate sheet. From left to right ratios d/L = 1 (repulsive), d/L = 2 (turning point) and d/L = 5 (attractive) are marked to Figure 4.2 with blue dots. The black lines are guide to the eyes and show the symmetry axis of the ε_{yy}.

4.3 Characteristic features

Figure 4.4 shows the typical paths of two plastic zones. Typically there are two clear regimes: attraction and repulsion. Figure 4.5 shows the characteristic times of selected features as a function of initial notch separation distance. The main feature is the turning time t_{turn} when repulsion turns to attraction

$$t_{turn} = arg\ max\ (y_1(t) - y_2(t)), \tag{4.1}$$

where y_1 and y_2 are y-coordinates of the upper and lower cracks respectively.

The most interesting result in Figure 4.5 is “the time” when MTSN changes direction. This is the time when local symmetry tells the crack to change direction. This also coincides with the time when the strain yy-component is at maximum. By definition, ε_{yy} and $\varepsilon_{\theta\theta}$ (hoop strain) are equal when $\theta = 0$. Note that in every case a clear maximum time can be found.

At the beginning of the experiment, the sample is at first elongated elastically. After a while the plastic zone starts to grow. In some cases with large horizontal initial distance L the plastic zone grows straight at first. This indicates that there is no interaction. This is not seen in all experiments. The crack starts to grow, soon after the plastic zone has grown to the flame shaped form seen in Figure 4.1. The crack grows inside the plastic zone until the sample starts to deform out of plane.

Common for all experiments is also the out of plane deformation soon after the crack tips have passed each other. The experiment is stopped at this point as the

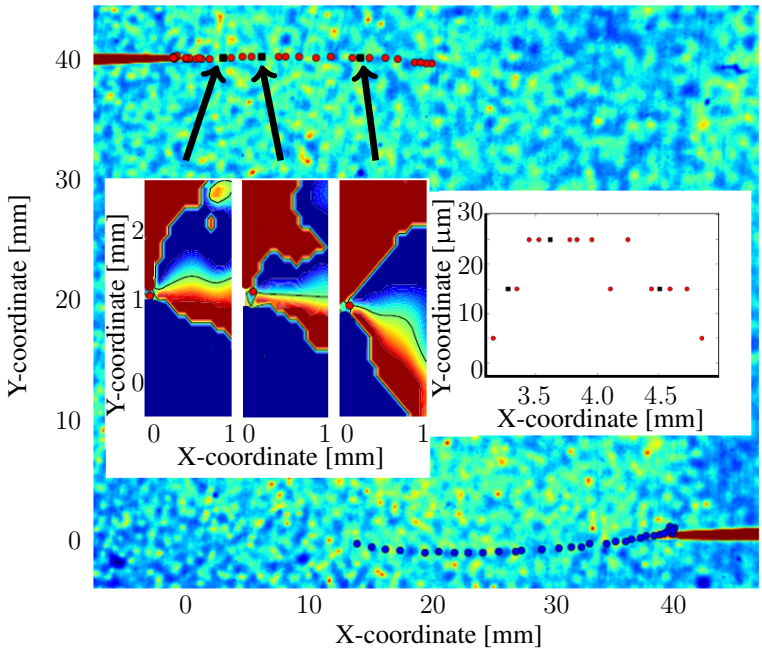

Fig. 4.4: A raw image (background) is overlayed with the plastic zone paths for both cracks (dots). The overlays show some displacement fields at chosen points (black dots). The overlay on the right shows a zoom to the upper plastic zone path.

digital image correlation does not measure strains of the material but the out of plane deformation. Usually at the same time as out of plane deformation starts a second plastic zone has been formed. The actual crack path and the path of the plastic zone tip are not the same. At the end of the experiment the crack tip hits the edge of the plastic zone and a new plastic zone starts to grow similarly as in the beginning of the experiment.

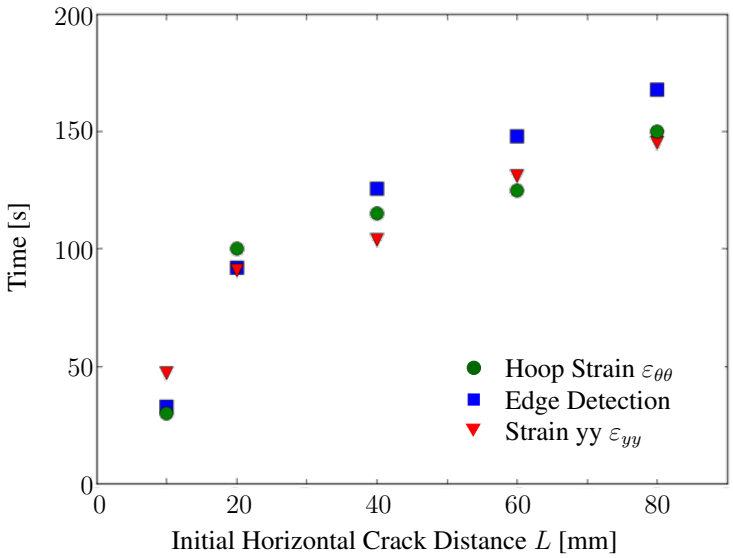

Fig. 4.5: Experiments with $d = 40$ mm have certain characteristic features that correlate with each other. The time of turning is taken from the plastic zone tip movement data, (blue dots) c.f. black dots in Figure 4.4. Strains yy ε_{yy} (red triangles) are from DIC as well as the turning points of MTSN (green circles).

4.4 Experimental propagation angle

The local symmetry argument essentially claims that the plastic zone will propagate to the direction where Mode II component vanishes. This can be measured in two ways: i) Find the location of maximum tangential strain or ii) find the symmetry axis in tangential displacement. The former method is theoretically more solid as the translational components vanish due to differentiation. The latter method however has less noise because it requires no differentiation, but suffers from two free parameters, $u_{x,t}$ and $u_{y,t}$. These parameters define the translational movement of the plastic zone tip due to the elastic elongation of the polycarbonate sheet. In other words a constant velocity is applied to the top edge of the sheet and the bottom edge does not move. The plastic zones thus have a constant speed upwards.

Figure 4.6 depicts the tangential strain during repulsion and attraction. The

plastic zone tip as the origin is marked with a black dot. Now, as it is mentioned in previous sections, the maximum tangential strain estimates the direction of the crack growth. In this case we claim that the plastic zone growth direction can be estimated as well. The Figure 4.6 shows clearly that this is the case. On the left, the maximum tangential strain $\varepsilon_{\theta\theta}$ points upwards, away from the other crack and the plastic zone paths repel each other at time $t = 50$ s. Later ($t = 125$ s on the right) the maximum tangential strain $\varepsilon_{\theta\theta}$ points downwards and the plastic zones attract each other. We can also see that the MTSN can be obtained far from the crack tip. The fluctuations or strain concentrations seen in the top right corner of the RHS Figure 4.6 might be due to some defects in the material or markers applied to the surface. It may also be possible that there are some residual strains from the beginning of the experiment. The maximum tangential strain was pointing this direction when the cracks were repelling each other.

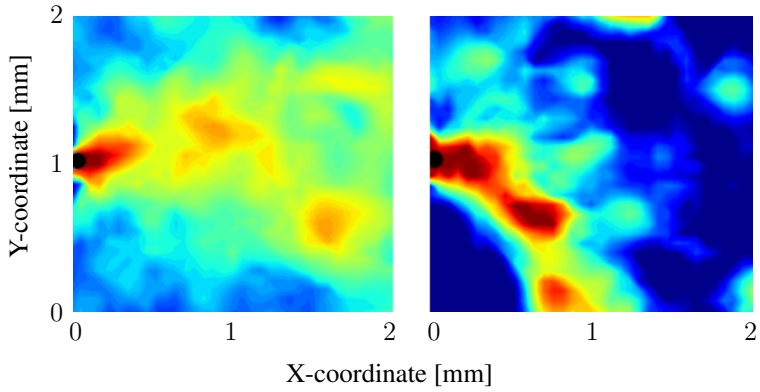

Fig. 4.6: Tangential strain, $\varepsilon_{\theta\theta}$ is plotted as contour plot during repulsion (left) and attraction (right) from the experiment where $d = 40$ mm and $L = 40$ mm. The image is zoomed at one of the crack tips. The other crack is out from the image area, lower right respect to the image. The plastic zone tip is $x = 0$ mm and $y = 1$ mm (black dot).

Similar to the tangential strain is the polar displacement ratio u_θ/u_r. This ratio has a few convenient characteristics. The lines when the nominator or the denominator are zero are clearly visible. The basic idea stays the same, the plastic zone propagates to the direction of local symmetry. The ratio u_θ/u_r is plotted as contour plot in Figure 4.7 at times $t = 90$ s (left) and $t = 155$ s (right). The red dot is representing the current location of the plastic zone tip as well as the origin of the polar coordinates. On the left hand side, a path where the ratio R is

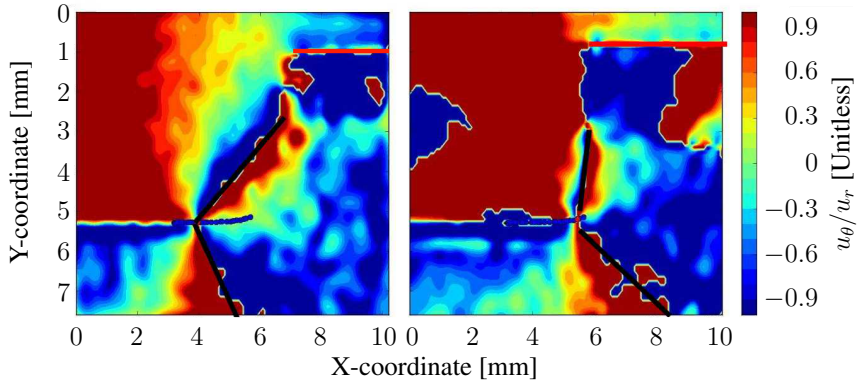

Fig. 4.7: u_θ/u_r from an experiment with $d = 40$ mm and $L = 40$ mm at time $t = 90$ s (left) and $t = 150$ s (right). The blue dots denote the plastic zone path. The Current location is marked with a red dot. The black lines are guides to the eye about where $u_r = 0$. The green area between the lines is the local symmetry area where the crack is expected to propagate. The second crack is marked with a red bar.

zero (green) emerges and goes straight, or slightly turns downwards, eventually turning upwards towards the crack number two. The second crack is marked with a red bar. The black lines represent the lines where denominator, u_r, goes to zero. These lines also suggest that the propagation direction is slightly downwards. The right hand side figure represents the same experiment as on the left but at a later time, t = 155 s. Here one can see that the path is now pointing upwards even in the vicinity of the plastic zone tip. This is seen as attraction in the plastic zone path. The $u_r = 0$ lines (black) also behave similarly.

Chapter 5

Devices and methods

This chapter describes the measurement devices and methods that are used to do the experiments in the latest papers. In the first section the digital image correlation analysis method is explained. The following sections describe the measurement system. The core is the expandable controller that was designed to put all devices behind the same start button. The goal is that during the measurement the experiment operator can concentrate on the samples, not the devices. The last three chapters introduce the tensile testing machine, camera and acoustic emission system. All of them can be coupled together via the controller.

5.1 Digital image correlation

The most labor intensive technique used in this thesis is Digital Image Correlation [48]. In its simplest form the goal is to find the transformation mapping between two digital images [49, 21, 50]. During the last ten years it has evolved from marginal to a main stream measurement technique. There exist turnkey solutions that can be integrated seamlessly to standard mechanical testing devices.

Roughly speaking, there exists two main categories how the analysis can be done. The main difference is how much analysis the DIC is performing during the correlation process. Cross correlation techniques rely on brute force while functional minimization methods are more sophisticated. The former are easy to implement and contain a small amount of tunable parameters. The drawbacks are the higher computational cost and a large number of outlayer points in results.

The easiest way to implement cross correlation is to use convolution in Fourier space. For example, with Python's scipy package the essential line is:

$$argmax(correlate2d(image1,\ image2\_roi)), \tag{5.1}$$

which returns the location (in image1) for region of interest taken from image2 (image2_roi). The rest is just file handling.

The functional methods reduce first the image dimensions by mapping the input images and result to smaller continuous functional bases. After reduction, standard minimization techniques can be used. The gains are faster algorithms and smooth results. The drawback is a larger amount of tunable parameters that require some prior knowledge of the problem at hand. A good example for this kind of problems is determining stress intensity factors [37]. The solution space is reduced to linear elastic displacement functions (low order terms in Williams series) and the result is directly the stress intensity factors.

The image correlation algorithm used mostly in this thesis is explained in detail in Reference [21]. It belongs to the functional minimization methods and uses b-splines as a basis for images and results. It requires two parameters, the spline degree and the size of the region of interest. These parameters determine the smoothness of the result.

5.2 Controller

The device relations are described in Figure 5.1. The purple arrows represent high speed data transfer. This is the raw unprocessed data that is streamed to storage. In this setup, all the data is stored and post processed. Only the acoustic emission recording has a time limitation of 1 to 2 minutes with full data collection rate that can be extended by online noise filtering. All the other devices can record hours or days of data with full speed.

The operating principle is simple. Instructions (green arrows) that are both human and machine readable are passed to each measurement computer. These computers convert the instructions to the (proprietary) formats that are understood by the corresponding measurement device. Some devices like humidity controller and heat bath require constant instructions. The purpose for these two devices is to manipulate environment either by changing air humidity (humidity controller) for humidity sensitive materials or water temperature (heat bath) in the case of water submerged samples. The standard operation procedure requires to give the setpoint value as voltage. Other devices, are mostly operated

in free run or trigger mode (black lines). Devices in free run mode typically require a set of instructions like “take 10 000 pictures with parameters X,Y,Z”. After the command the device does not need any other inputs.

The data produced by the devices is transferred with high speed (purple lines) to the local measurement computer and stored. The data is then shared to a common location.

The measurement computers have an option to send reduced human readable information back to viewer computer (yellow arrows), that can be the same as the controller (or even your cell phone). This helps evaluating whether the experiment will be successful or not.

The above pattern is called Model-view-control [51], where the model is a set of measurement computers. The advantage is the independence of complex programs that makes the system expandable. The drawback is the requirement for the extra communication interface.

If the measurement device has a reasonable interface, adding a new device takes usually less than an hour. The AE system was installed in 45 minutes and the water heat bath in 30 minutes. Adding and removing devices can be done online and requires no changes to algorithms. This makes it possible to develop the system simultaneously with the measurements.

5.3 Tensile testing machine

The most important device is the Instron E1000 tensile testing machine. It can apply 1000 N of force and is capable of cyclic waveforms up to 100 Hz. The main program that operates tensile testing machine is written with Labview, shown in Figure 5.2. This pattern is called factory method. For each given keyword, the program decides which protocol it returns. For this protocol *init* and *run* methods are run. This utilizes *inheritance* in Object Oriented Programming. All protocols inherit the methods from the *General Protocol* -object, namely *init* and *run*.

Figure 5.3 shows the tensile testing machine compressing wood. In the typical setup there is the imaging device (d) that is either a normal or an infrared camera, grips (a,b) that in this figure are compression plates and a load cell (c) that measures the applied load.

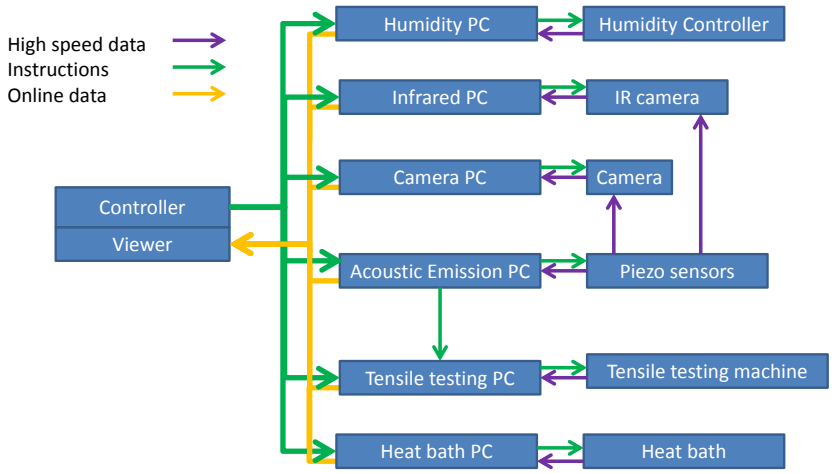

Fig. 5.1: Measurement devices are connected to a central computer via a measurement computer containing the viewer and the controller.

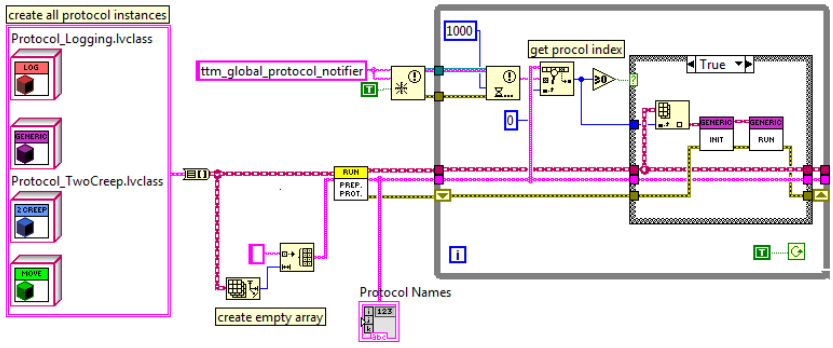

Fig. 5.2: A Labview code block illustrates how the measurement protocols are loaded into the cluster (pink box on the left). Users trigger notifiers to launch protocols by init and run commands.

5.4 Camera

The digital camera is the fastest 1 megapixel camera that requires no external hardware. Dalsa HM1024 takes 117 frames per second at full resolution of 1024 x 768 pixels. The amount of data fills the bandwidth of a gigabit Ethernet cable that is used to connect the camera. Camera software was developed in the bachelor's thesis of Jani Saarenpää [52].

The future developement can include image based triggering. Field-programmable gate array chips and calculations with graphical processing units are coming to market with a user friendly programming interface. This makes it possible to use high speed image correlation in a feedback loop. Currently, there exists a demoversion in our lab that calculates the local strains of the sample with one second delay. This data can also be used to control the tensile testing machine.

5.5 Acoustic emission

During a fracture process elastic energy is released. Part of that energy goes to mechanical vibration that can can be observed as acoustic emission. Recently this was used in compression fracture [53]. The standard way is to measure the signal with piezocrystal sensor. The technique is based on piezoelectricity that converts the mechanical changes of the material into a voltage difference. The simplest piezoelectric device is two conductive parallel surfaces. Changing the distance between the surfaces changes the capacitance and thus the voltage between the surfaces. In crystals, the surfaces are polarized crystal planes and very close to each other.

Recently, new methods have been developed. VTT has developed new acoustic emission measurement microelectromechanical sensor (MEMS) devices based on changes in capacitance between the silicon disc and a surface. The difference is that MEMS devices resonate only with one specific frequency. An example of single acoustic emission event from paper creep experiment measured with piezo crystal sensor is seen in Figures 5.4. The acoustic emission system and differences between traditional and MEMS AE sensor are explained in more detail in Ari-Pekka Honkanen's bachelor thesis [54].

An acoustic emission feedback loop was developed in order to control the tensile testing machine with AE-signal. The Instron E1000 has the ability to take external signal as control signal. 1 second delay in feedback was implemented by Eetu Pursiainen in his bachelor's thesis [55] and this is being improved by Tero Mäkinen during his bachelor's project.

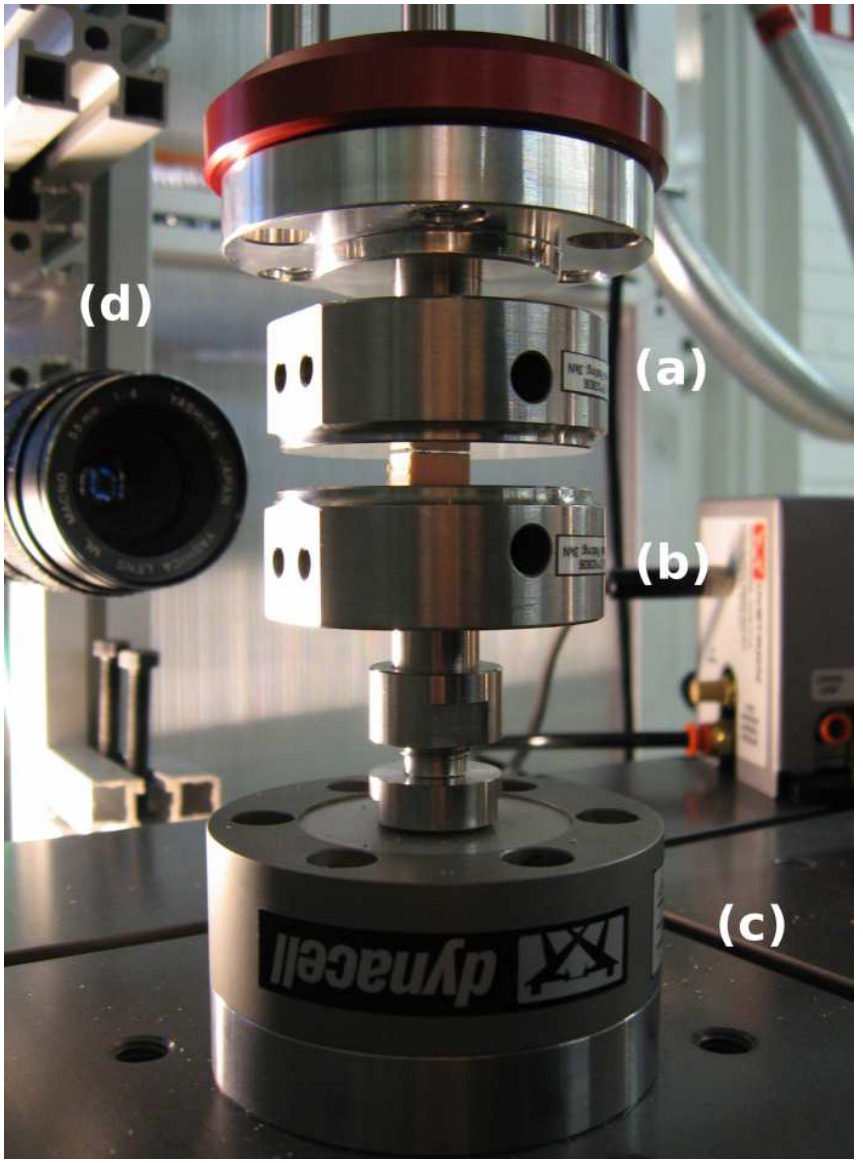

Fig. 5.3: The tensile testing machine is starting to compress wood between compression plates (a) and (b). The force is measured load sensor (c). The digital camera (d) records the compression process.

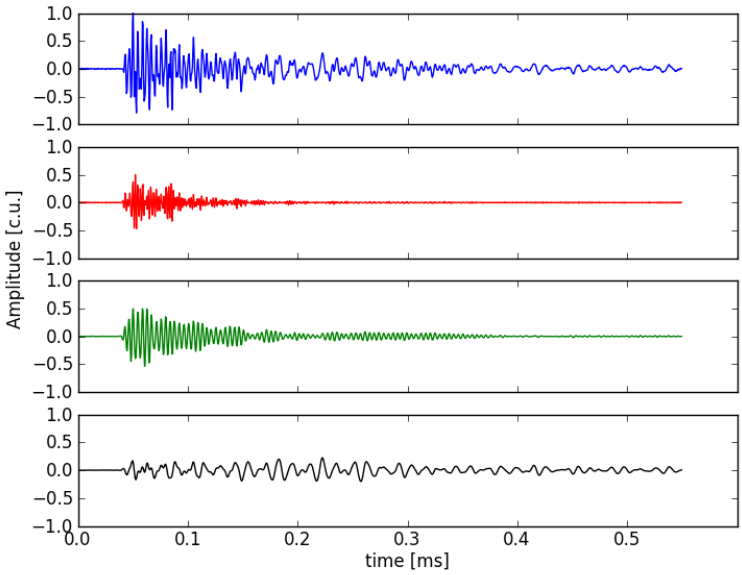

Fig. 5.4: A typical AE event (blue) is split into high (red), middle (green) and low (black) frequency parts.

The idea of the feedback is to convert intermittent dynamics to a smooth control signal for the tensile testing machine. The experiments can be then done e.g. with constant acoustic emission rate. This allows to study the correlation and the clustering of events. Preliminary results show that the energy distribution does not change, but there is change in waiting time distributions.

The simplest way to do this is to decrease the force or displacement ramp (pulling speed) if there is acoustic activity. In similar fashion the ramp is increased in the case of no acoustic emission. This method allows roughly 1 second feedback delays. A more sophisticated feedback method is to reverse the computer - testing machine interaction by creating event listeners. In the above method, the computer was the master, telling to the testing machine when to increase or decrease the ramps. The other way is to make the testing machine the master that requires more control points from the slave computer. The slave constantly creates control points that are read by the master when it wants to read them. This reduces the feedback delay to 100 ms or so.

Chapter 6

Conclusions

The topic of this thesis is fracture propagation and prediction. Chapters 2 and 4 relate to fracture propagation and in Chapter 3 it is described how the strains, both global and local, can be used to predict the failure. The last chapter introduces the measurement system that was developed during this thesis.

6.1 Driven manifolds in a random potential

In Chapter 2 it is described how a 1d fracture line in paper behaves. It is found that there exists a depinning transition. The elastic kernel can be shown to be long range kind which is something one would expect. Using a short range kernel however produces a similar disorder correlator function as with long range kernels after normalization. Together with the third cumulant, there is a difference. This indicates that the avalanche shapes are different. And the experiments coincide more with the long range simulations.

The future research regarding the peeling experiment could include more detailed measurement of clustering of events. The fracture front is macroscopic, 30 mm wide. Even if the elasticity is non-local, do the events belong to the same avalanche, or is there multiple avalanches that are just happening at the same time. Also, a small portion of the events might be completely uncorrelated background noise. For instance, the large inter event waiting times might be compromised by even small amount of random events.

6.2 Fluctuations and prediction

A series of experiments to obtain 2d strain data was made to measure creep properties. Standard tensile creep experiments revealed a crucial role of fluctuations in paper fracture. The secondary Andrade creep highlights the increasing role of fluctuations; the standard deviation of strain rate decays slower than the average strain rate. This means that the strain is concentrating to few spots. These strain concentrations can be used to predict the failure of the sample at the beginning of the experiment. The length of the primary creep and the magnitude of the fluctuations correlate with the lifetime. Also, the Monkman-Grant relation applies to paper creep, even if the load or loading protocol is changed.

The primary and secondary creep are observed in a wide range of materials as is the Monkman-Grant relation. Future research topics could include for instance changing the disordered material to e.g. nanofibre-reinforce plastics and checking the universality of the predictability; Does the transition from primary creep to secondary creep correlate with lifetime? Does a large strain concentration at the beginning mean a short lifetime?

6.3 Fracture

In the crack growth experiment in Chapter 4, it is shown for the first time in the case of curved cracks that the local symmetry path is the path that the crack essentially follows. The path can be extracted from displacements or from strains. In the experiments at hand, the focus was to obtain a method that allows the examination the validity of $K_{II} = 0$ path. Already in the elastic region of polycarbonate sheets, the described methods work currently only by showing the direction where the crack will propagate next. It is an open question how far from the crack tip the prediction is valid.

In the case of viscous and heterogeneous materials like paper, the disorder plays even more significant role. Preliminary results show that in the case of one crack there might be multiple paths were $K_{II} = 0$ due to heterogeneity. The question is if the crack path can even be predicted. Paper deformation has a viscous component that acts as a memory. This could be seen as residual strains which affect the measured strain fields, especially in the case when the cracks are turning.

In the of plastics a photoelasticity measurement allows the examination of stress [35]. Together with digital image correlation or particle image velocimetry, both

stress and strain could be measured simultaneously. This allows the (dis)validation of energy based crack propagation criteria.

Bibliography

[1] S. Semaw, P. Renne, J. W. Harris, C. S. Feibel, R. L. Bernor, N. Fesseha, and K. Mowbray, *2.5-million-year-old stone tools from Gona, Ethiopia*, Nature **385**, 333 (1997).

[2] L. Salminen, M. Alava, and K. Niskanen, *Analysis of long crack lines in paper webs*, The European Physical Journal B **32**, 369 (2003).

[3] K. J. Schrenk, N. A. M. Araújo, J. S. Andrade, and H. J. Herrmann, *Fracturing ranked surfaces*, Scientific Reports **2**, 348 (2012).

[4] M. Alava and K. Niskanen, *The physics of paper*, Reports on Progress in Physics **69**, 669 (2006).

[5] M. Marder, *Cracks cleave crystals*, Europhysics Letters **66**, 364 (2004).

[6] J. Rosti, J. Koivisto, X. Illa, P. Traversa, J.-R. Grasso, and M. J. Alava, *Line creep in paper peeling*, International Journal of Fracture **151**, 281 (2008).

[7] J. Koivisto, J. Rosti, and M. J. Alava, *Creep of a fracture line in paper peeling*, Physical Review Letters **99**, 145504 (2007).

[8] P. Chauve, T. Giamarchi, and P. Le Doussal, *Creep and depinning in disordered media*, Physical Review B **62**, 6241 (2000).

[9] P. Le Doussal, K. J. Wiese, S. Moulinet, and E. Rolley, *Height fluctuations of a contact line: A direct measurement of the renormalized disorder correlator*, Europhysics Letters **87**, 56001 (2009).

[10] K. J. Måløy, S. Santucci, J. Schmittbuhl, and R. Toussaint, *Local waiting time fluctuations along a randomly pinned crack front*, Physical Review Letters **96**, 45501 (2006).

[11] J. Heierli and M. Zaiser, *Failure initiation in snow stratifications containing weak layers: Nucleation of whumpfs and slab avalanches*, Cold Regions Science and Technology **52**, 385 (2008).

[12] D. S. Fisher, *Collective transport in random media: from superconductors to earthquakes*, Physics Reports **301**, 113 (1998).

[13] L. I. Salminen, A. I. Tolvanen, and M. J. Alava, *Acoustic emission from paper fracture*, Physical Review Letters **89**, 185503 (2002).

[14] L. I. Salminen, J. M. Pulakka, J. Rosti, M. J. Alava, and K. J. Niskanen, *Crackling noise in paper peeling*, Europhysics Letters **73**, 55 (2006).

[15] A. Tanguy, M. Gounelle, and S. Roux, *From individual to collective pinning: Effect of long-range elastic interactions*, Physical Review E **58**, 1577 (1998).

[16] P. Le Doussal and K. Wiese, *Size distributions of shocks and static avalanches from the functional renormalization group*, Physical Review E **79**, 051106 (2009).

[17] D. C. Dunand, B. Q. Han, and A. M. Jansen, *Monkman-Grant analysis of creep fracture in dispersion-strengthened and particulate-reinforced aluminum*, Metallurgical and Materials Transactions A **30**, 829 (1999).

[18] E. N. D. C. Andrade, *On the viscous flow in metals, and allied phenomena*, Proceedings of the Royal Society Of London Series A **84**, 1 (1910).

[19] D. W. Coffin, *The creep response of paper*, 13th Fundamental Research Symposium, Cambridge, UK, pp. 651 – 747 (2005).

[20] J. Rosti, J. Koivisto, L. Laurson, and M. J. Alava, *Fluctuations and scaling in creep deformation*, Physical Review Letters **105**, 100601 (2010).

[21] M. Mustalahti, J. Rosti, J. Koivisto, and M. J. Alava, *Relaxation of creep strain in paper*, Journal of Statistical Mechanics: Theory and Experiment **P07019**, (2010).

[22] L. Laurson, S. Santucci, and S. Zapperi, *Avalanches and clusters in planar crack front propagation*, Physical Review E **81**, 46116 (2010).

[23] M. C. Miguel, A. Vespignani, S. Zapperi, J. Weiss, and J. R. Grasso, *Intermittent dislocation flow in viscoplastic deformation*, Nature **410**, 667 (2001).

[24] A. Miksic, J. Koivisto, and M. Alava, *Statistical properties of low cycle fatigue in paper*, Journal of Statistical Mechanics: Theory and Experiment **P05002**, (2011).

[25] C. Manzato, A. Shekhawat, P. K. V. V. Nukala, M. J. Alava, J. P. Sethna, and S. Zapperi, *Fracture strength of disordered media: universality, interactions, and tail asymptotics*, Physical Review Letters **108**, 065504 (2012).

[26] M. Alava, P. Nukala, and S. Zapperi, *Role of disorder in the size scaling of material strength*, Physical Review Letters **100**, 055502 (2008).

[27] S. Lennartz-Sassinek, M. Zaiser, I. G. Main, C. Manzato, and S. Zapperi, *Emergent patterns of localized damage as a precursor to catastrophic failure in a random fuse network*, Physical Review E **87**, 042811 (2013).

[28] T. Shrestha, M. Basirat, I. Charit, G. P. Potirniche, and K. K. Rink, *Creep rupture behavior of grade 91 steel*, Materials Science and Engineering: A **565**, 382 (2013).

[29] H. T. Hahn, J. L. Timmer, J. Bartley-Cho, S. Lee, and S.-G. Lim, *The effect of preloading on fatigue damage in composite structures, Part I*, Federal Aviation Administration, Office of Aviation Research, (1996).

[30] I. G. Main, *A damage mechanics model for power-law creep and earthquake aftershock and foreshock sequences*, Geophysical Journal International **142**, 151 (2000).

[31] S. Pradhan and P. C. Hemmer, *Prediction of the collapse point of overloaded materials by monitoring energy emissions*, Physical Review E **83**, 041116 (2011).

[32] F. Kun, F. Raischel, R. C. Hidalgo, and H. J. Herrmann, *Modelling critical and catastrophic phenomena in geoscience - A statistical physics approach*, Lecture Notes in Physics **705**, 1 (2006).

[33] R. Hidalgo, F. Kun, and H. Herrmann, *Creep rupture of viscoelastic fiber bundles*, Physical Review E **65**, 032502 (2002).

[34] B. Cottrell and J. R. Rice, *Slightly curved or kinked cracks*, International Journal of Fracture **16**, 155 (1980).

[35] K. Sakaue, S. Yoneyama, and M. Takashi, *Study on crack propagation behavior in a quenched glass plate*, Engineering Fracture Mechanics **76**, 2011 (2009).

[36] A. Livine, E. Bouchbinder, and J. Fineberg, *Breakdown of linear elastic fracture mechanics near the tip of a rapid crack*, Physical Review Letters **101**, 264301 (2008).

[37] J. Réthoré, S. Roux, and F. Hild, *Mixed-mode crack propagation using a hybrid analytical and extended finite element method*, Comptes Rendus Mécanique **338**, 121 (2010).

[38] J. Réthoré, S. Roux, and F. Hild, *Hybrid analytical and extended finite element method (HAX-FEM): A new enrichment procedure for cracked solids*, International Journal for Numerical Methods in Engineering **81**, 269 (2009).

[39] M. B. Nooru-Mohammed, *Mixed-mode fracture of concrete: an experimental approach*, PhD Thesis, Technische Universiteit Delft, (1992).

[40] B. Patzák and M. Jirásek, *Adaptive resolution of localized damage in quasi-brittle materials*, Journal of Engineering Mechanics **130**, 720 (2004).

[41] P.-P. Cortet, L. Vanel, and S. Ciliberto, *Surface oscillations and slow crack growth controlled by creep dynamics of necking instability in a glassy film*, The European Physical Journal E **27**, 185 (2008).

[42] K. Mróz and Z. Mróz, *On crack path evolution rules*, Engineering Fracture Mechanics **77**, 1781 (2010).

[43] S. K. Maiti and R. A. Smith, *Comparison of the criteria for mixed mode brittle fracture based on the preinstability stress-strain field part I: Slit and elliptical cracks under uniaxial tensile loading*, International Journal of Fracture **23**, 281 (1983).

[44] M. Kachanov, *Elastic solids with many cracks and related problems*, Advances in Applied Mechanics **30**, 259 (1993).

[45] T. Seelig and D. Gross, *On the interaction and branching of fast running cracks - a numerical investigation*, Journal of Mechanics and Physics of solids **47**, 945 (1999).

[46] S. Melin, *Why do cracks avoid each other?*, International Journal of Fracture **23**, 37 (1983).

[47] M. L. Fender, F. Lechnault, and K. E. Daniels, *Universal shapes formed by two interacting cracks*, Physical Review Letters **105**, 125505 (2010).

[48] M. A. Sutton, J. L. Turner, H. A. Bruck, and T. A. Chae, *Full-field representation of discretely sampled surface deformation for displacement and strain analysis*, Experimental Mechanics **31**, 168 (1991).

[49] B. Pan, K. Qian, H. Xie, and A. Asundi, *Two-dimensional digital image correlation for in-plane displacement and strain measurement: a review*, Measurement Science and Technology **20**, 062001 (2009).

[50] F. Mathieu, F. Hild, and S. Roux, *Identification of a crack propagation law by digital image correlation*, International Journal of Fatigue **36**, 146 (2012).

[51] E. Gamma, R. Helm, R. Johnson, and J. Vlissides, *Design patterns: Elements of reusable object-oriented software*, Addison-Wesley, Boston (1994).

[52] J. Saarenpää, *High frequency digital image correlation in primary creep*, BSc Thesis, Aalto University, Espoo, (2010).

[53] J. Baro, A. Corral, X. Illa, A. Planes, E. K. H. Salje, W. Schranz, D. E. Soto-Parra, E. Vives, J. Baró, and A. Corral, *Statistical similarity between the compression of a porous material and earthquakes*, Physical Review Letters **110**, 088702 (2013).

[54] A.-P. Honkanen, *Measuring acoustic emission from paper under tensile testing*, BSc Thesis, University of Helsinki, Helsinki, (2012).

[55] E. Pursiainen, *Akustiseen emissioon perustuva ohjaus paperin rasituskokeissa (Loading protocol for paper based on acoustic emission)*, BSc Thesis, Aalto University, Espoo, (2011).

Aalto-DD 122/2013

ISBN 978-952-60-5275-5
ISBN 978-952-60-5276-2 (pdf)
ISSN-L 1799-4934
ISSN 1799-4934
ISSN 1799-4942 (pdf)

Aalto University
School of Science
Department of Applied Physics
www.aalto.fi

BUSINESS +
ECONOMY

ART +
DESIGN +
ARCHITECTURE

SCIENCE +
TECHNOLOGY

CROSSOVER

**DOCTORAL
DISSERTATIONS**